Rock Mech Rock Eng (2016) 49:2479–2501
DOI 10.1007/s00603-015-0889-5

ORIGINAL PAPER

Investigation of Geomorphic and Seismic Effects on the 1959 Madison Canyon, Montana, Landslide Using an Integrated Field, Engineering Geomorphology Mapping, and Numerical Modelling Approach

A. Wolter[1] · V. Gischig[2,4] · D. Stead[3] · J. J. Clague[3]

Received: 15 December 2014 / Accepted: 4 November 2015 / Published online: 26 November 2015

Abstract We present an integrated approach to investigate the seismically triggered Madison Canyon landslide (volume = 20 Mm^3), which killed 26 people in Montana, USA, in 1959. We created engineering geomorphological maps and conducted field surveys, long-range terrestrial digital photogrammetry, and preliminary 2D numerical modelling with the objective of determining the conditioning factors, mechanisms, movement behaviour, and evolution of the failure. We emphasise the importance of both endogenic (i.e. seismic) and exogenic (i.e. geomorphic) processes in conditioning the slope for failure and hypothesise a sequence of events based on the morphology of the deposit and seismic modelling. A section of the slope was slowly deforming before a magnitude-7.5 earthquake with an epicentre 30 km away triggered the catastrophic failure in August 1959. The failed rock mass rapidly fragmented as it descended the slope towards Madison River. Part of the mass remained relatively intact as it moved on a layer of pulverised debris. The main slide was followed by several debris slides, slumps, and rockfalls. The slide debris was extensively modified soon after the disaster by the US Army Corps of Engineers to provide a stable outflow channel from newly formed Earthquake Lake. Our modelling and observations show that the landslide occurred as a result of long-term damage of the slope induced by fluvial undercutting, erosion, weathering, and past seismicity, and due to the short-term triggering effect of the 1959 earthquake. Static models suggest the slope was stable prior to the 1959 earthquake; failure would have required a significant reduction in material strength. Preliminary dynamic models indicate that repeated seismic loading was a critical process for catastrophic failure. Although the ridge geometry and existing tension cracks in the initiation zone amplified ground motions, the most important factors in initiating failure were pre-existing discontinuities and seismically induced damage. Amplification played a secondary role.

Keywords Madison Canyon landslide · Engineering geomorphology mapping · Endogenic and exogenic processes · Dynamic modelling in UDEC · Topographic and damage amplification · Seismic fatigue

1 Introduction

Large catastrophic rockslides are among the most damaging and dangerous natural hazards. Much research has focussed on understanding their mechanisms and related processes, with the ultimate aim of predicting and mitigating future events. Conditioning factors can be separated into exogenic and endogenic processes. Exogenic processes, such as weathering, mass wasting, fluvial incision, and glacial erosion, are those that damage a rock mass due to climatic and gravitational forcing. Endogenic processes, such as tectonics, isostasy, volcanism, and seismicity, are those that damage a rock mass due to the Earth's geodynamic system (Gerber and Scheidegger 1969; Whalley 1974; Leith 2012).

The context, or situation, of an unstable slope is important in understanding failure initiation and

✉ A. Wolter
awolter@ethz.ch

[1] Engineering Geology, ETH Zürich, Zurich, Switzerland

[2] Earth and Ocean Sciences, University of British Columbia, Vancouver, BC, Canada

[3] Earth Sciences, Simon Fraser University, Burnaby, BC, Canada

[4] Present Address: Swiss Competence Centre for Energy Research (SCCER-SoE), ETH Zürich, Zurich, Switzerland

propagation. Engineering geomorphology is the application of geomorphological theory and methods to engineering projects. It provides spatial context for engineering works and allows engineers to assess the impact of engineering on the environment and landscape, and to evaluate the risks and implications of landform change to humans (Giardino and Marston 1999; Lee et al. 2004; Fookes et al. 2005, 2007; Griffiths et al. 2012). Griffiths and Whitworth (2012) applied the concept of the geomorphological process-response system to landslides, wherein mass movements are part of a larger system of processes and landforms contributing to the four-dimensional evolution of a landscape. Their approach is part of the larger engineering geomorphology framework pioneered by Brunsden et al. (1975), Doornkamp et al. (1979), the Geological Society of London (1982), and Fookes et al. (2005, 2007).

The significant influence of seismicity on natural slope stability has long been recognised. Although considerable research has been conducted on earthquake-triggered landslides, the interaction between seismic waves and slopes is not well understood (Murphy et al. 2002; Murphy and Mankelow 2004; Saygili and Rathje 2009; Wasowski et al. 2011). Seismicity is commonly assumed to be short-term dynamic loading that affects slopes, reducing their stability (Meunier et al. 2007). In reviewing the literature, we have noted that the long-term effects of multiple earthquakes, earthquake types, epicentral distance and travel path, directional effects, dispersion, and incoherence on slope integrity are rarely considered.

In this paper, we back-analyse the 1959 Madison Canyon landslide in Montana, USA, using the endogenic-exogenic process framework to better understand the conditioning factors that led to catastrophic failure. We focus on geomorphic and seismic processes, and examine landforms and their evolution. We also examine seismic wave amplification due to topographic or internal damage as well as seismic history. We integrate structural geology, engineering geomorphology, and preliminary dynamic modelling in a forensic investigation of the catastrophic failure. The main objectives of this research are to (1) understand the interaction between endogenic and exogenic processes affecting the Madison Canyon slope, and how they condition the slope for failure; (2) determine the effects of seismic waves on the slope; and (3) establish the evolution of the slope and the landslide through time and the sequence of events leading up to and including the catastrophic failure.

2 Background

The Madison Canyon landslide (Fig. 1) was triggered by the largest historic earthquake in the Rocky Mountains ($M = 7.5$) on August 18, 1959. It involved a volume of 20 Mm^3 of schist, gneiss, and dolomitic marble that fragmented while travelling rapidly downslope. The rockslide killed 26 people and dammed Madison River, creating Earthquake Lake. The slide occurred on the steep southern valley wall at the mouth of Madison Canyon, at the front of the Madison Range. This orogenic belt is situated within the Intermountain Seismic Belt, which is dominated by shallow seismicity due to differential motions among the Juan de Fuca, Pacific, and North American plates to the west. Seventy-seven earthquakes were recorded and felt between 1869 and 1959 in the Yellowstone-Hebgen Lake area, and several active faults attest to the high level of historic seismic activity in the region (Fig. 1; Doser 1985). The Hebgen and Red Canyon normal faults east of the landslide reactivated during the 1959 earthquake sequence.

The Hebgen Lake region has short warm summers and long cold winters, with an average annual rainfall of 250–450 mm (Hadley 1978); the relief in the area is 1500 m (1900–3400 m asl). At the time of the Madison Canyon failure, the region and presumably the slope were dry.

The V-shaped profile of the Madison River valley and the lack of remnant glacial landforms at the canyon mouth indicate that its slopes have not been glaciated. Ten kilometres upstream of the landslide site, however, a large hummocky moraine covers the valley floor. De la Montagne (1960) and Shelden (1960) suggest that the Madison Range was affected by local alpine glaciers during the last two Pleistocene glaciations.

3 Methods

In spite of the loss of life and its impacts on the valley floor, the Madison Canyon landslide has not been extensively studied (Hadley 1964, 1978; Kent 1966; Trunk et al. 1986; Jibson 2009). We applied modern techniques, including terrestrial digital photogrammetry and dynamic numerical modelling, to study the landslide. We integrated geomorphologic observations and engineering geomorphologic mapping with field and photogrammetric discontinuity surveys and rock strength estimation (Fig. 2). The results provided input and constraints for subsequent numerical analyses.

We constructed post-event engineering geomorphology maps based on analysis of 1959 aerial photographs and fieldwork in 2011 and 2012. In the field, we measured breaks and changes in slope with a clinometer along transects oriented roughly NNE-SSW and spaced 50 m apart (Fig. 3). Mapping was completed according to Geological Society of London (1982) guidelines, with two types of maps produced: (1) morphometric maps showing breaks and changes in slope; and (2)

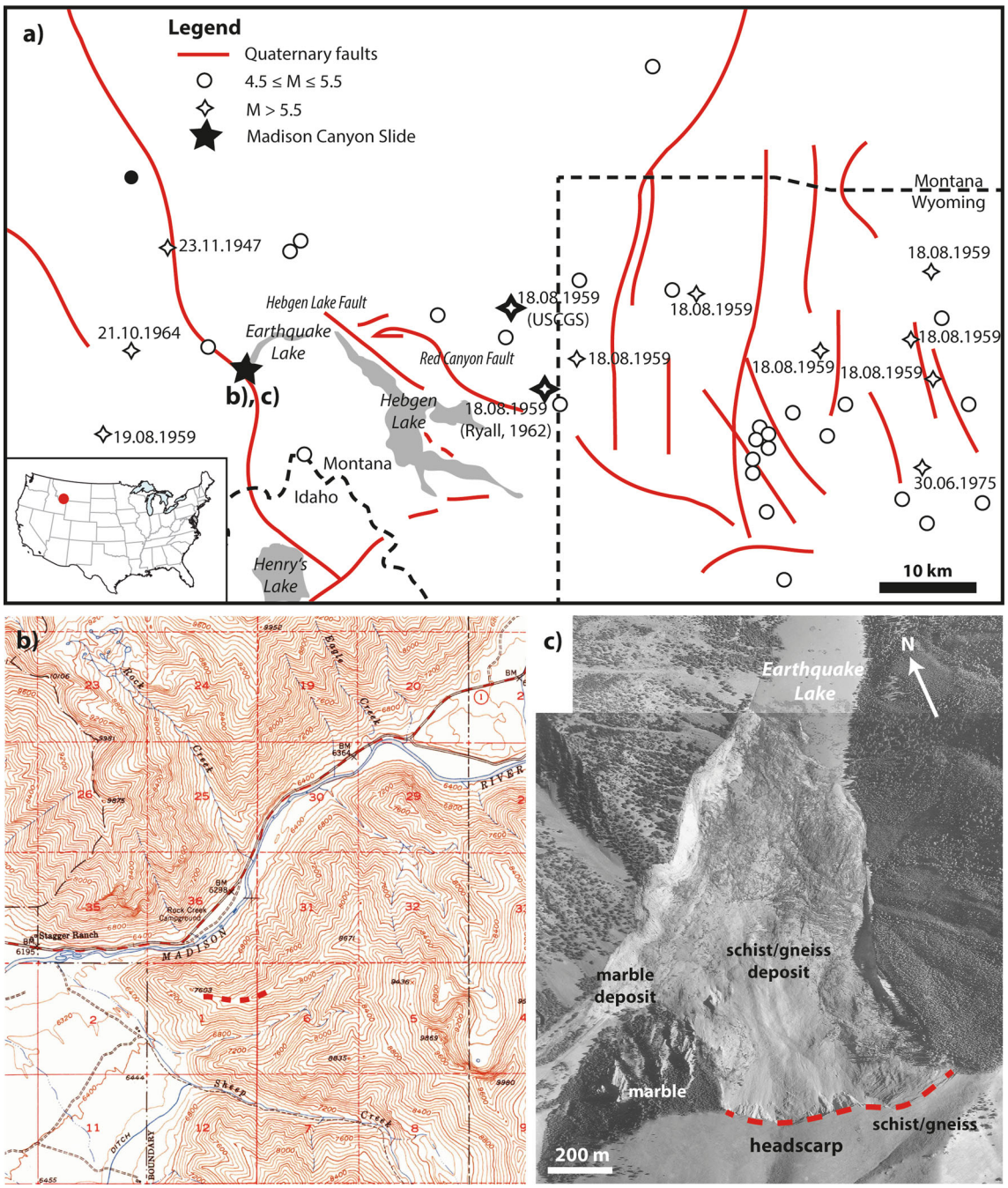

Fig. 1 Location and tectonic context of the Madison Canyon landslide in southern Montana, USA. **a** Fault and historic seismic map of the Hebgen Lake area (modified from Doser 1985), showing historic earthquakes with dates (dd.mm.yyyy) if known. The two accepted epicentres of the main 1959 event—those of the US Coast and Geodetic Survey and Ryall (1962)—are indicated by *bold larger diamonds*. Note the number of aftershocks (other points with the same date). The *black star* shows the location of the Madison Canyon landslide and the area covered by **b** and **c**. **b** 1950 (pre-slide) US Geological Survey topographic map of the Madison Canyon area with the future headscarp marked with a *dashed red curve* (*scale* 1 square = 1750 m). **c** 1959 US Geological Survey aerial photograph of the Madison Canyon landslide shortly after it happened, showing the slide characteristics (colour figure online)

morphogenetic maps illustrating our interpretations of the descriptive maps, from which we derived relations among landforms within the slide area and inferred processes operating on the slope.

Using a series of historical US Geological Survey aerial photographs, we reconstructed the evolution of the site of the Madison Canyon landslide. Features such as gullies, scarps, tension cracks, Madison River, marble outcrops,

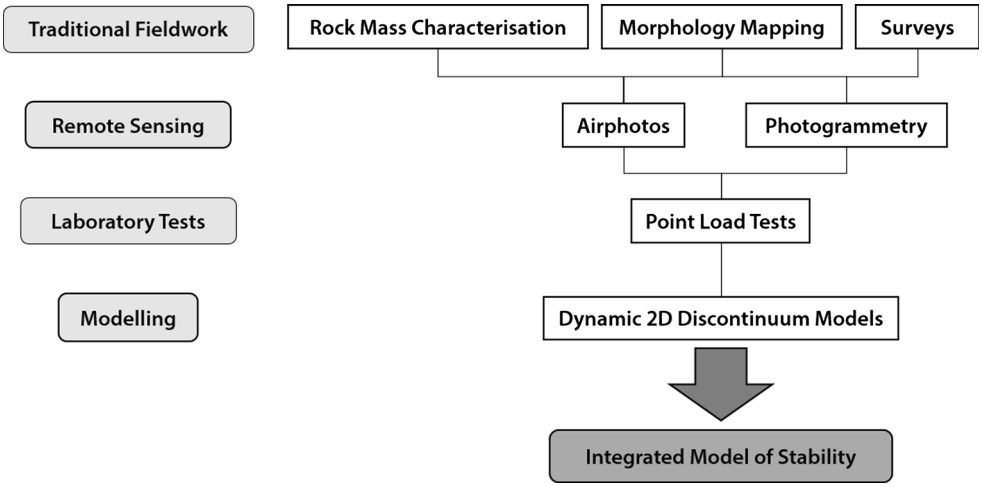

Fig. 2 Flowchart of the integrated methodology used to study the Madison Canyon landslide

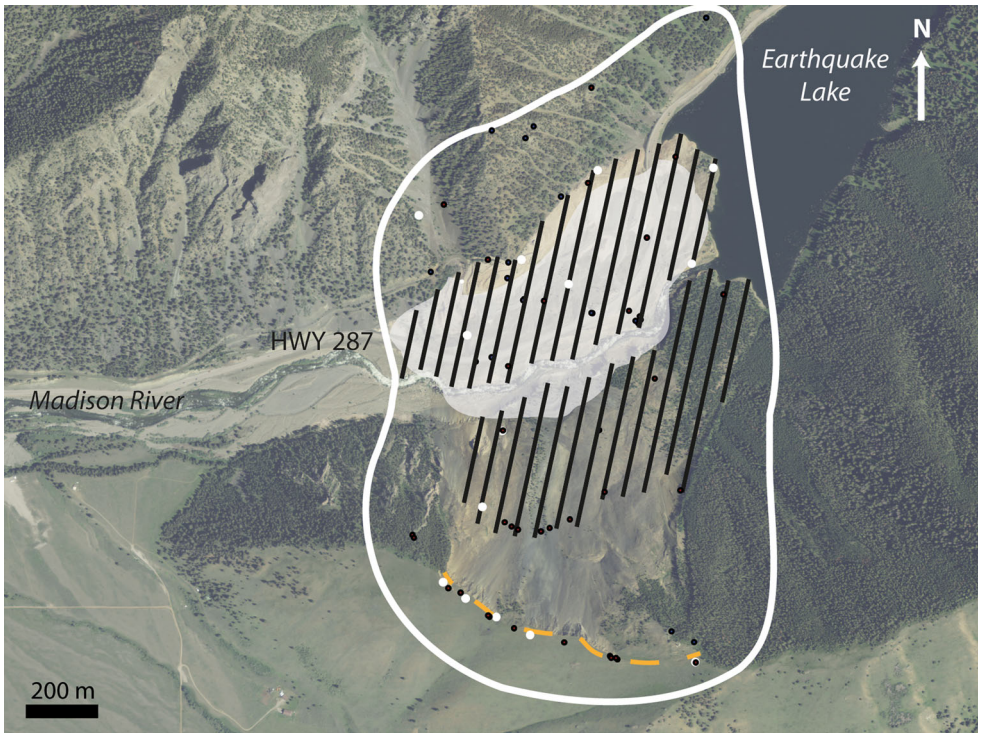

Fig. 3 Approximate locations of transects (*black lines*) used to map the morphology of the Madison Canyon landslide deposit. The area beneath the headscarp was inaccessible. The *white curve* outlines the study area; the *white polygon* indicates the area that has been anthropically modified; and the *golden dashed curve* delineates the headscarp. *Black dots* indicate field stations at which in situ characterisation was completed; *white dots* are locations where point load samples were also collected (colour figure online)

and mass movements were mapped on georeferenced photographs taken in 1947, 1954, 1959 (both before and after the landslide), 1976, 1982, and 2002.

Rock mass characterisation techniques included field and photogrammetric discontinuity line surveying; estimation of field hammer strength, weathering grade, block size and shape, and Geological Strength Index (GSI) (Hoek et al. 1995; Marinos and Hoek 2000); and laboratory point load testing. We characterised and sampled both in situ rock masses and landslide debris, as indicated in Fig. 3. Point load and hammer test results, in combination with typical strength values for similar rock types reported in the literature (RocData, Rocscience 2013), were used to estimate numerical modelling property input values. The long-range terrestrial photogrammetry surveys, the first of such undertaken at the Madison Canyon landslide, were created and processed using the methodology presented in Sturzenegger (2010).

After running static numerical models on the landslide, we conducted preliminary dynamic stress-deformation analyses using the two-dimensional distinct element code UDEC (v. 6.0; Itasca 2014) to investigate the role of seismicity at Madison Canyon. Two aspects of the impact of seismicity on the Madison Canyon slope were

Table 1 Models run in UDEC to investigate seismic wave amplification and damage effects at Madison Canyon

Model set	Geometry	Materials	Discontinuities[a]	Seismic input	Model number
I. Amplification	Straight	Schist	None	Ricker wavelets	1–8
		Schist + marble	Con	f_D = 0.1–10 Hz	9–16
	Concave	Schist	None	Ricker wavelets	17–24
		Schist + marble	Con	f_D = 0.1–10 Hz	25–32
	Convex	Schist	None OR ss	Ricker wavelets	33–48
		Schist + marble	Con	f_D = 0.1–10 Hz	49–56
			Con + ss + TCs		57–64
II. Damage	Convex	Schist + marble	Con + ss + vor φ_{ss_peak} = 10–30° φ_{vor_peak} = 15–35° c_{ss_peak} = 0.1–1 MPa c_{vor_peak} = 1–10 MPa	Nisqually M = 6.8	65–78
			Con + ss + DS φ_{ss_peak} = 10–35° φ_{DS_peak} = 15–40° c_{ss_peak} = 0–1 MPa c_{DS_peak} = 0–5 MPa	Nisqually M = 6.8	79–99
			Con + ss + vor	5 earthquakes M = 5.3–6.8	100–102
			Con + ss + DS	5 earthquakes M = 5.3–6.8	103–105

Con schist/marble contacts, *ss* sliding surface, *TCs* tension cracks, *vor* Voronoi, *DS* discontinuity sets

[a] Ranges in friction angle and cohesion properties indicate values used for models in which sensitivity analyses were conducted

investigated (Table 1):(1) amplification of seismic waves due to topography and pre-existing discontinuities; and (2) progressive weakening of the slope rock mass induced by multiple earthquakes, which conditioned the slope for failure.

For both series of models, we used the parameters in Tables 2 and 3, based on Itasca (2014) recommendations. In these preliminary dynamic analyses, rigorous calibration of parameters was not undertaken (Alzo'ubi 2009; Kazerani and Zhao 2010; Gao 2013), given data limitations on the rock strength and rock mass properties. Before starting the dynamic simulations, we ran each model to an initial static equilibrium state. Because in situ stress measurements are unavailable for the Madison site, as a first approximation and based on our investigative models and Hoek et al. (2011), stress boundaries and initial stress conditions were selected to simulate an in situ stress ratio of $k = 1$. To prevent seismic wave reflections, we applied absorbing free-field boundaries to the sides and a viscous boundary to the base of each model after static equilibrium had been reached. Each seismic input history (ground velocity) was converted to transient stress boundary conditions to simulate the seismic disturbance of the slope.

In the first series of dynamic models, which focus on seismic amplification, we selected three model geometries—straight, concave, and convex—based on a representative profile of the Madison Canyon slope. Simulations were run using (1) elastic, one-material (schist), non-jointed or jointed models; and (2) elastic, two-material (schist and marble), jointed models (models 1–64; Table 1). The "intact" schist and marble materials were defined by density (ρ), and shear (G) and bulk (K) moduli (Fig. 4). Models included the assumed failure surface and tension cracks (Fig. 4) based on observations from pre-1959 air photographs, previous publications (Hadley 1964, 1978), and the results of our engineering geological mapping. Tension fractures and the sliding surface were modelled as highly compliant discontinuities with low stiffness values (Table 3), after the procedure proposed by Moore et al. (2011, 2012). Given their well-defined spectral content, Ricker wavelets with a range of dominant frequencies—f_D = 0.1, 0.5, 1, 2, 5, 8, and 10 Hz—were used as input for the UDEC dynamic slope models. The method for evaluating amplification is similar to that used by Bourdeau and Havenith (2008) and Gischig et al. (2015a, b), where amplification is calculated as the ratio between wave

Table 2 Model properties and conditions for dynamic simulations in UDEC, following Itasca (2014) recommendations

Property	Value/description
Material constitutive behaviour	Elastic
Joint constitutive behaviour	Coulomb slip with peak and residual values
Damping	Rayleigh (mass and stiffness proportional)
$\xi_{\min}$	0.001–0.01
$f_{\min}$	2 Hz
Mesh size	18 m
Side boundaries	Free-field
Basal boundary	Viscous + stress (wave input)

Table 3 Discontinuity properties used in the UDEC dynamic simulations. Initial values were used for the marble contacts throughout modelling

Property	Initial properties	Sliding surface		Tension cracks	Voronoi/DS	
		Peak	Residual		Peak	Residual
Friction angle (°)	50	35	15	30	40–10	35–5
Cohesion (MPa)	50	10–0	0	5	15–0	0
Tensile strength (MPa)	17	1.5–0	0	0	5–0	0
Normal stiffness (GPa/m)	100	1	1	1	1	1
Shear stiffness (GPa/m)	10	0.1	0.1	0.1	0.1	0.1

DS discontinuity sets

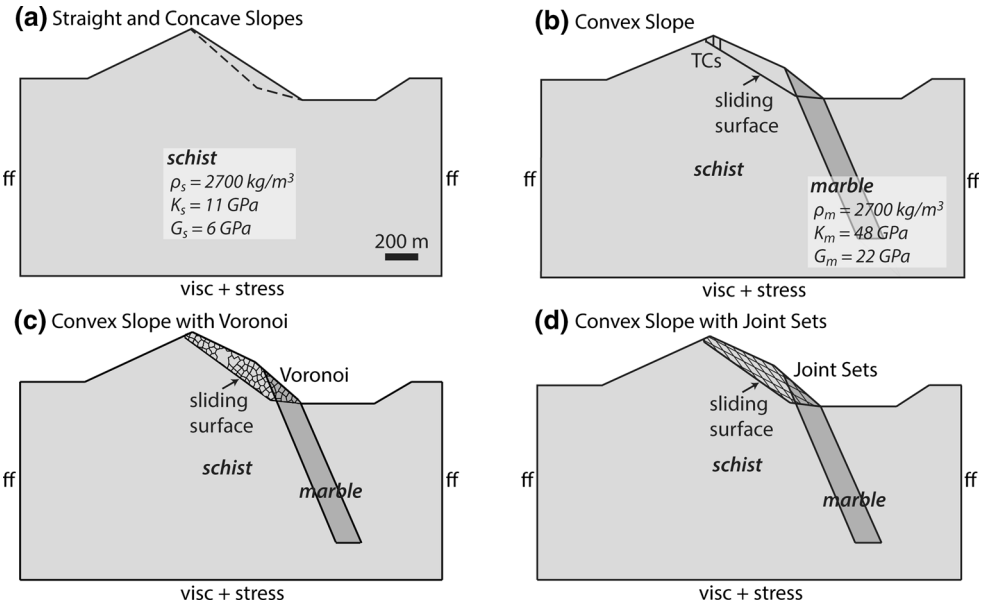

Fig. 4 Modelling geometry for the dynamic UDEC simulations. $\rho_{s(m)}$ density of the schist (marble) "intact" material; $K_{s(m)}$ bulk modulus of the schist (marble) material, $G_{s(m)}$ shear modulus of the schist (marble) material, *ff* free-field boundaries, *visc* viscous (quiet) boundaries, *TC* tension crack. **a**, **b** Models used for amplification investigations. **c** The Voronoi model set including the sliding surface and marble contacts as discontinuities, and **d** the discontinuity set model set (see Tables 1, 2, 3 for model properties)

spectra at the model ground surface and the original input signal at the model base. We computed spectral amplification curves obtained using this approach for a dense array of observation points at the surface (spacing 20 m). Patterns showing amplification as a function of space and frequency could then be computed.

In the second series of dynamic models (models 65–105; Table 1), we investigated the role of rock mass damage in the failure using two geometries. We first used Voronoi tessellation in the convex slope geometry to simulate dynamically induced brittle fracturing in the slope mass, with polygons with an average edge length of 30 m (Fig. 4c). This was the minimum possible Voronoi size, given mesh element size, which was constrained by modelling time limitations. Note that we interpret fractures in Voronoi models as showing general stress-induced damage, not as indicating where actual fractures formed in the slope. Fractures in the models are defined as Voronoi surfaces or discontinuities that have reached their strength threshold, either through tension or shear, and now have residual

Table 4 Earthquake records used in the UDEC seismic sequence model subset

Record	M	I_A (m/s)	$D_{5–95\ \%}$ (s)	PGA (g)	PGV (cm/s)	D_e (km)	D_f (km)	Site	Focal mechanism
1994 Northridge	6.7	0.841	7.4	0.232	16.1	14.7	22.8	Rock	Reverse
1957 Daly City	5.3	0.055	3.7	0.112	4.6	11.1	13.7	Rock	Reverse
2001 Nisqually	6.8	0.276	25.2	0.155	6.3	15.6	54.7	Rock	Normal
1986 N. Palm Springs	6.1	0.063	7.7	0.106	2.6	49	50.2	Rock	Oblique reverse

M moment magnitude, I_A Arias intensity, $D_{5–95\ \%}$ Dobry duration (time required to build up the central 90 % of the Arias intensity, *PGA* peak ground acceleration, *PGV* peak ground velocity, D_e epicentral distance, D_f focal distance

strength properties (Table 3). Then, using models without Voronoi but with two discontinuity sets from field investigations (foliation and DS2), we simulated discontinuity-controlled block failure and fracture propagation due to seismic activity (Fig. 4d). In one subset of both the Voronoi and discontinuity set models, we conducted sensitivity analyses on cohesion and friction angle values to determine at which shear strength values the slope would fail when only one earthquake (the Nisqually, Washington, 2001 record) was applied to the model. In the cohesion sensitivity models, peak cohesion of the Voronoi (vor) or set (DS) fractures was reduced from 10 MPa to 0 MPa and peak cohesion of the sliding surface (ss) was reduced from 1 to 0.1 MPa. In the friction angle sensitivity models, the peak friction angle of the Voronoi or set fractures was reduced from 40° to 15° and the peak friction angle of the sliding surface was reduced from 35° to 10°. In the second subset of models (models 100–105; Table 1), we applied a sequence of five earthquakes (magnitudes 5.3–6.8) to models with different strength properties ($c_{vor/DS\_peak} = 2.5$ MPa, $c_{ss\_peak} = 0.25$ MPa, $\varphi_{vor/DS\_peak} = 30°–40°$, $\varphi_{ss\_peak} = 25°–35°$), using ground motions from the SLAMMER database (Table 4; Jibson et al. 2014) to determine how much seismic damage would be required to cause the slope to fail. The sequence was chosen based on Doser's (1985) database of historic earthquakes in the Hebgen Lake area (Fig. 1a).

4 Results

4.1 Engineering Geomorphology Mapping and Geomorphological Evolution

4.1.1 Aerial Photograph Map

Analysis of engineering geomorphology maps and aerial photographs allowed us to interpret landform change. The 1959 morphogenetic map (Fig. 5), based on air photographs taken immediately after the landslide, highlights several features of the landslide, including the headscarp, debris lithology, and structures in the debris related to landslide kinematics.

The headscarp strikes roughly WNW-ESE, is 800-m long, and can be separated into four zones. The westernmost, 170-m-long section is steep (>50° slope angles), about 30 m high, and is dominated by exposed schist-gneiss (zone 1 in Fig. 5). To the east of this area, the second section of the scarp (zone 2) is 160-m long and comprises a secondary slump. It forms a saddle between the higher steeper scarps on both sides and coincides with a dry gully on the south side of the ridge. The third section (zone 3) is a wedged-shaped scarp 240-m long and up to 50 m high with >50° slopes, some of which overhang. The easternmost section (zone 4) is 230-m long and is the source of a large secondary slump. The lateral scarps of the landslide dip >45° and are oriented approximately N-S. The east lateral scarp is about 500-m long, whereas the west scarp is 250-m long. Although the scarps do not appear to be controlled by major structures, the headscarp coincides with foliation in the schist and gneiss, and the lateral scarps are parallel to major N-S trending normal faults in the region.

The surface of the debris sheet is marked by transverse ridges and longitudinal and transverse lineations, which may have important implications for the slide kinematics and movement behaviour. Figure 6 shows areas of compression and extension in the landslide area, based on the ridges and lineations observed and other geomorphological features. Conspicuous transverse ridges near the northeast margin of the debris are both sinuous and rounded, and may be compressional structures associated with thrust faulting (Shea and van Wyk de Vries 2008). These 50- to 500-m-long ridges have metre- to decametre-scale amplitudes, and are oriented roughly NW–SE to NNE-SSW (Fig. 7a). They are orthogonal to the NE direction of movement of the debris at this location. Some of the ridges support trees that were tilted and toppled during movement.

Longitudinal lineations occur in clusters at two locations in the distal debris—one cluster of 21 lineations occurs south of a lighter crushed schist band, which is 50 m south of the ribbon of marble (Fig. 5). A second, smaller cluster of three lineations is in the northeast part of the deposit. The longitudinal lineations are probably associated with internal shearing and strike-slip displacements of the debris

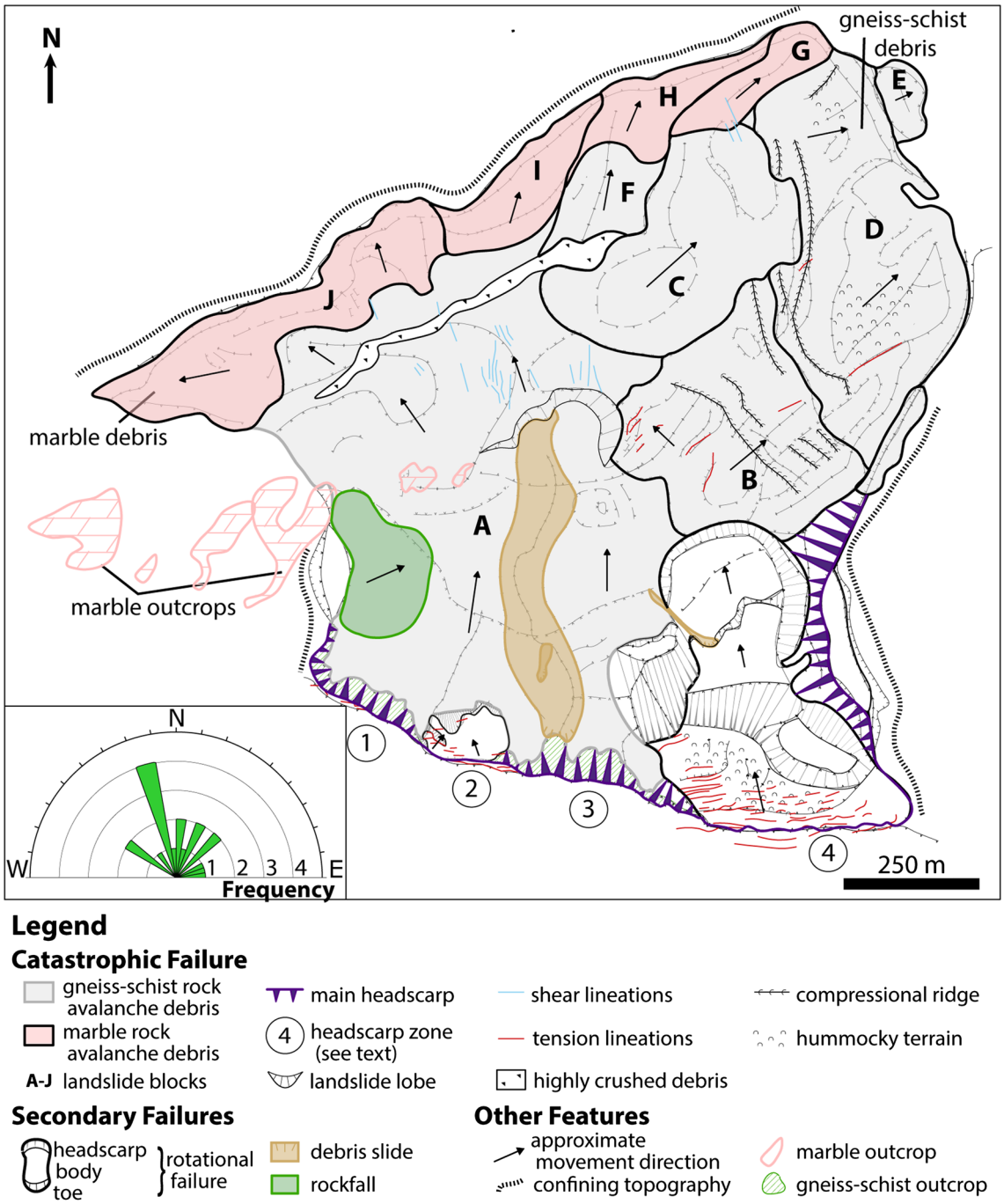

Fig. 5 Morphometric and morphogenetic map of the Madison Canyon landslide based on interpretation of the 1959 air photographs. *Inset* movement vector orientations (colour figure online)

during transport. The lineations are parallel to flow, with SE-NW (150°/330°) to NNE-SSW (007°/187°) trends, and are several tens of metres long (Fig. 7b). They resemble longitudinal stripes noted in the debris of other rock avalanches, such as the 2002 Black Rapids rock avalanches in Alaska (Shugar and Clague 2011).

Transverse lineations are tension cracks related to normal faulting and are most common in the headscarp area and at the crests of secondary slumps that occurred shortly after the main rock avalanche event. Most of these lineations are in zone 4 of the headscarp (Fig. 5) and appear to be related to slow deformation of the secondary slump there. Another cluster occurs in zone 2 of the headscarp, again associated with a secondary slump. Some longitudinal tension cracks are present in the central-east area of the deposit and are likely related to secondary movements

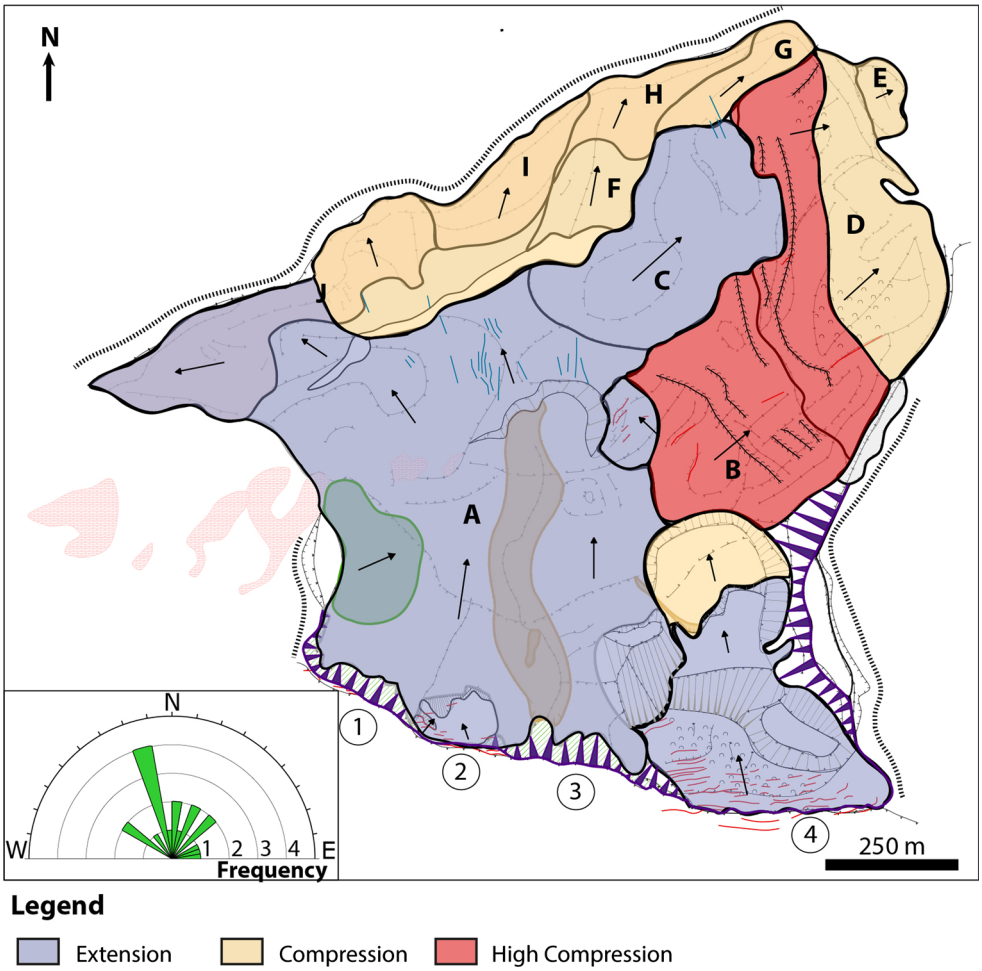

Fig. 6 Map of areas of extension and compression at Madison Canyon based on lineations and ridges (see text) (colour figure online)

after the main rock avalanche event. The transverse lineations range in length from 5 to 90 m, and in orientation from NNE-SSW (012°/192°) to WSW-ENE (155°/335°) (Fig. 7b), suggesting movement directions of NW to NNW.

The deposit includes areas of undulating to hummocky terrain, particularly below zone 4 and in the northeast part of the deposit where compressional ridges are present. The terrain near the headscarp appears to have formed due to extension, whereas the terrain in the northeast part of the debris sheet probably reflects compressional stresses within the deposit (Fig. 6).

Marble debris forms a linear band up to 100-m wide at the outer limit of the debris sheet. As this debris band extends to the far eastern end of the debris sheet, it appears that marble was exposed near the base of the slope farther to the east than today. The presence of marble at the debris front suggests that the sliding surface must have gone through the in situ marble. The preservation of the stratigraphy in the deposit indicates a fairly laminar, non-turbulent mechanism of movement on the slope scale.

Based on differences in morphology, tree cover, and intact character of the rock, we subdivided the debris sheet into ten blocks or domains, labelled A to J in Fig. 5. The most apparent division, other than the lithological boundary between the schist and marble debris, is the boundary between the highly fragmented and dispersed debris typical of a rock avalanche deposit to the west and the less fragmented, more intact rock material to the east. The largest domain (A), roughly 500-m wide by 750-m long, is characterised by highly fragmented debris with shear flow lines at its distal end. Material in this domain moved to the NNE and NNW (Fig. 5, inset). This domain is bordered to the east by more coherent, less fragmented blocks. Domain B is mostly vegetated, with sinuous ridges indicating compression and movement to the ENE. Minor secondary movements to the NNW, indicated by extensional lineations in the northwest corner of the domain, probably occurred after initial emplacement. Domain C is a broad circular high area bordered by a depression at its northeast margin. Shear lineations cross-cut the boundary between domains C and G. Domain D is another vegetated, more

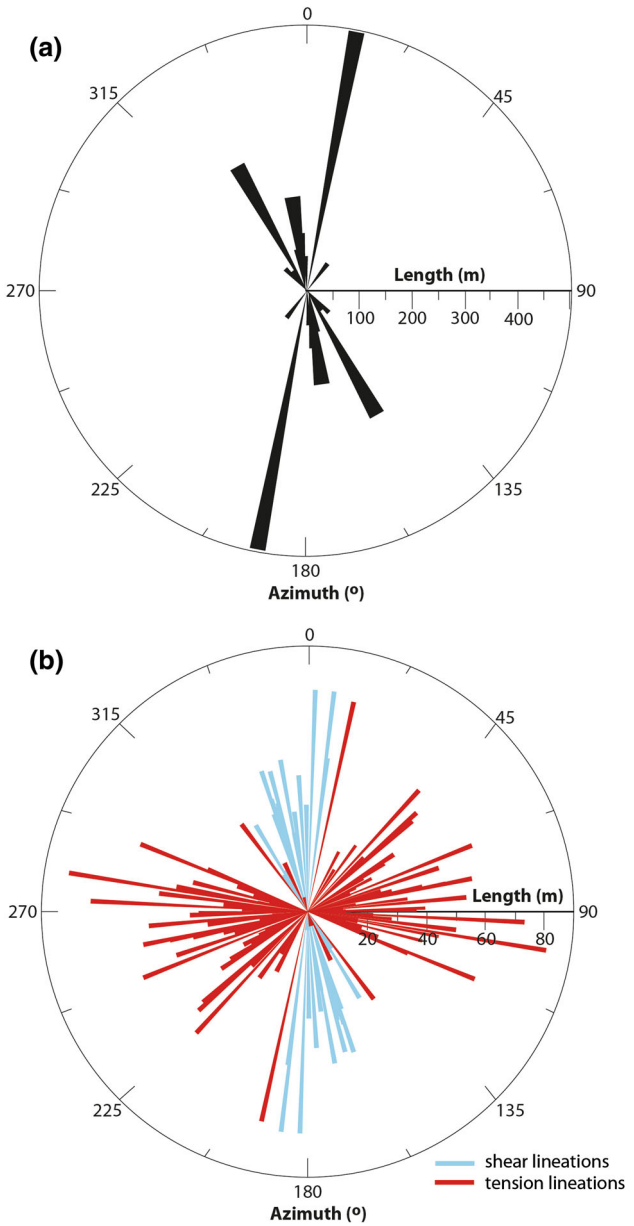

Fig. 7 Polar plots of feature trend and length for **a** compressional ridges and **b** shear and tension lineations in the Madison Canyon landslide deposit. Locations of features are indicated in Fig. 5

coherent zone. Ridges in this domain are sinuous and located at the rear of the domain, suggesting compression in response to collision with material behind it. A ridge at the northeast corner of domain D indicates compression due to collision with the leading edge of the slide (domain G). Domain E is a smaller, secondary block that has separated from domain D and moved to the east. Domain F is a small ridged zone that moved to the NNE and is separated from domains A and C by shear surfaces. Domains G, H, I, and J comprise the band of marble at the leading edge of the Madison Canyon landslide. The divisions between them are shear zones. Domains G, H, and I moved NE, and domain J moved NE to NW.

4.1.2 Morphometric Field Map of the Landslide

A sample of the detailed morphometric field map, which is found in its entirety in Wolter (2014), is shown in Fig. 8. The morphometric map, when compared with the 1959 map, shows how the landslide has evolved over the past 50 years. Modification of the debris has been extensive, particularly on the north bank of Madison River. Highway 287 crosses the debris, and a visitor centre, parking lot, and paths have been constructed on the debris sheet. Parallel linear ridges and gravel roads were constructed to access building material on the south side of the river. Boulders of marble were moved to the river, as the US Army Corps of Engineers used them to armour the river channel to prevent erosion. The largest, house-sized marble block, near the margin of the debris sheet, is designated the "Memorial Boulder" in commemoration of those killed by the landslide.

4.1.3 Evolution of the Landslide and Landscape

Gullies aided in georeferencing and delineating the failure, especially at its east margin (Fig. 9). Gullies unaffected by the 1959 landslide have not changed over the period spanned by the photographs (1947–2002) and appear to terminate in midslope positions. Comparison of pre- and post-slide photographs indicates that two gullies coincided with the east lateral margin of the landslide.

Several tension cracks and scarps are visible in the pre-slide photographs, mainly near the ridge crest and on the south-facing slope of the ridge. The most conspicuous scarps are just to the east of the slide and indicate a larger area of instability than involved in the 1959 catastrophic failure. A few scarps are visible on the 1947 and 1954 photographs. As illustrated on the 1959 map (Fig. 5), the number of extension lineations increased dramatically when the landslide occurred. Since 1959, the number of lineations visible on photographs has not changed. During field mapping in 2011 and 2012, we observed small fresh fractures, mainly near the western end of the headscarp (zone 1 in Fig. 5) and in the saddle area (zone 2). The unstable area appears to be expanding toward the west.

Marble crops out on the south slope of Madison Canyon in the form of unvegetated, castellated ridges separated by gullies. The ridges are oriented downslope (approximately N-S) and are several decametres in length. The contact between the marble and schist units in the slide area is a plane of weakness that may have been part of the west lateral release surface in the upper part of the slope.

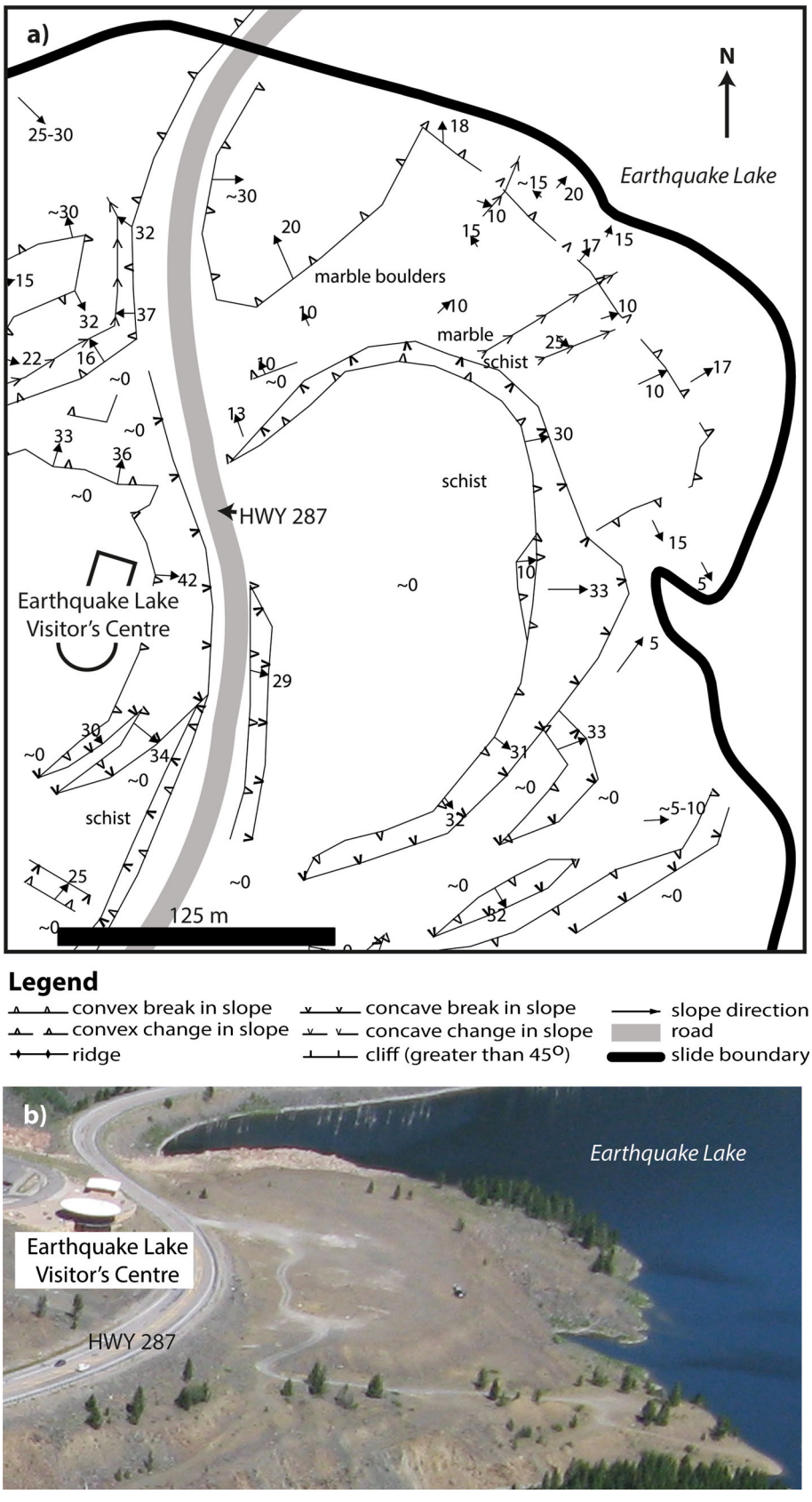

Fig. 8 **a** Sample of the field morphometric map showing slope directions and angles, and breaks and changes in slope. **b** Photograph of the mapped area at the northeast corner of the debris sheet

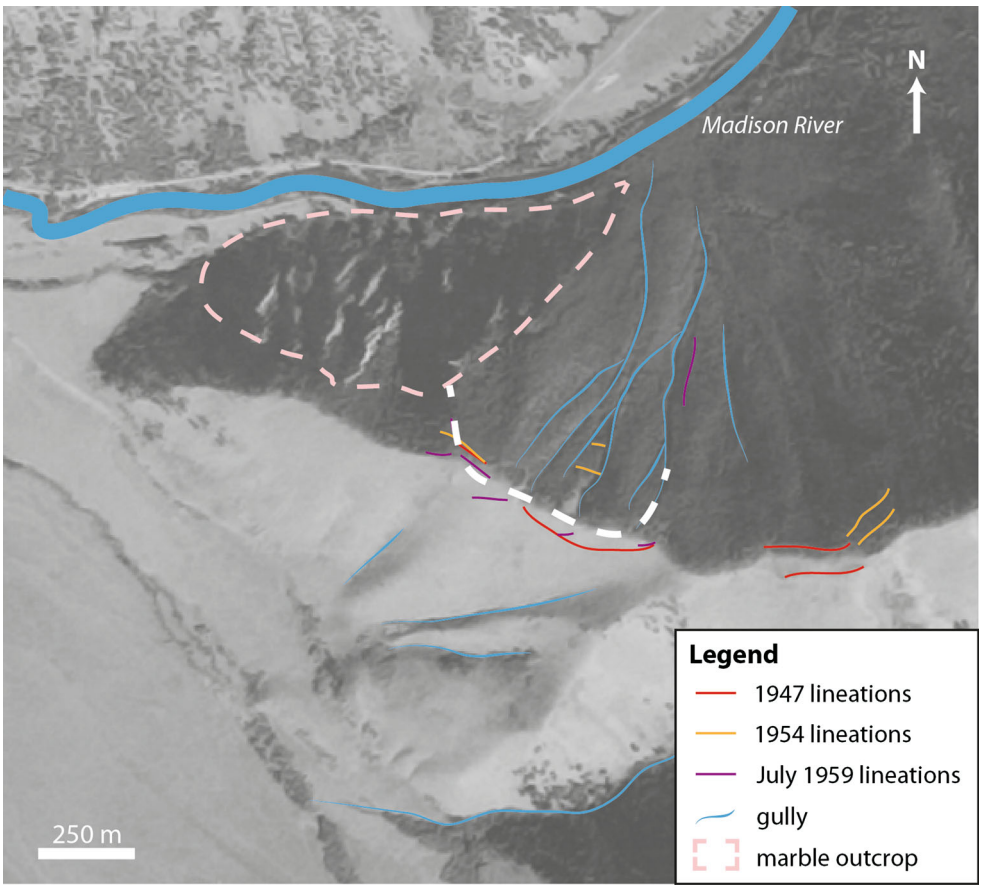

Fig. 9 Lineations, gullies, Madison River, and marble outcrops mapped on the 1947, 1954, and pre-event 1959 US Geological Survey air photographs. The *white dashed curve* is the approximate location of the headscarp of the Madison Canyon landslide. Base photograph is the 1954 air photograph (courtesy of US Geological Survey) (colour figure online)

Although there is no evidence of large failures in the slide area prior to 1959, we identified several potential debris slides, slumps, and rockfalls on the pre-slide photographs, indicating a longer history of mass movements. The possible debris slide scars are located east of the 1959 slide area but on the same slope. Debris flows travelling down Rock Creek on the opposing valley side have formed a large fan where the creek meets Madison River. The fan has deflected the river against the opposite valley wall, the site of the Madison Canyon landslide.

4.2 Rock Mass and Debris Characterisation

Based on field observations, we separated the study area into two lithostructural domains (I and II), corresponding to the schist and marble units. We did not observe folds or faults in outcrops or other variability such as joint set or rock mass changes within each unit that would warrant further division of the domains. From field and photogrammetric surveys, we identified five discontinuity sets (DS), including foliation, in the schist domain and eight sets in the marble outcrops (Table 5). Most foliation planes are smooth and planar to undulating; some surfaces, however, are slickensided, rough, wavy, and stepped. The foliation is also crenulated on the centimetre scale. Trace length values range from <2 to >20 m for all sets, with a maximum measured length of 26 m. Although we found

Table 5 Summary of the discontinuity sets (DS) identified in the field and photogrammetric models

DS	Dip (°)	Dip direction (°)
Foliation	49	342
1	40	112
2	70	246
3	73	37
4	65	72
1[a]	54	344
2[a]	72	86
3[a]	45	240
4[a]	43	97
5[a]	84	146
6[a]	84	205
7[a]	55	24
8[a]	89	304

Orientations represent averages from both sets of data

[a] DS associated with the marble

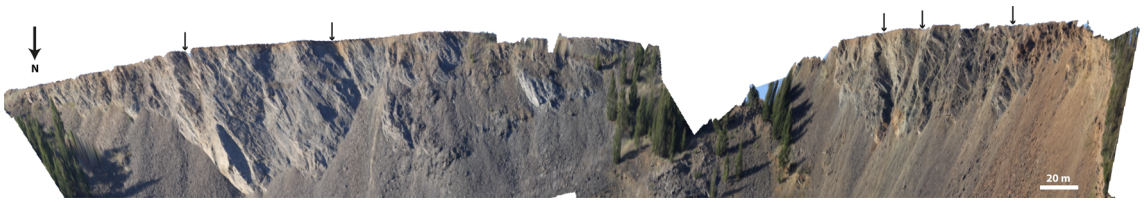

Fig. 10 Photogrammetric model (focal length lens $f = 200$ mm) of the Madison Canyon landslide headscarp showing the wedges constituting the composite rear release surface. *Arrows* indicate the locations of some of the wedges

joint-bounded blocks in the debris, the discontinuity sets do not appear to have controlled the failure behaviour in 1959. Local, small-scale wedges controlled by the intersection of the foliation planes and DS 1 are visible in the headscarp area (Fig. 10) and form composite rear and lateral release surfaces in the schist. The discontinuity orientations in the marble are more variable, and the unit is highly fractured. Based on Kalenchuk et al.'s (2006) block shape classification system, the schist blocks can be described as platy or elongated-platy and the marble blocks as cubic or cubic-elongated. Average block sizes in the in situ and transported schist are approximately 0.01 and 0.012 m^3, respectively. The average in situ marble block is 0.009 m^3, whereas the average transported marble block is 0.02 m^3. Transported schist and marble blocks are generally larger north of Madison River, suggesting that larger blocks were transported on a matrix of finer material at the deposit front. Secondary failures may also have transported finer material from the headscarp to the middle of the deposit south of the river. The larger block size in the debris highlights the likely importance of weathering and seismic damage—pre-landslide rock outcrops are likely to be more fractured and weathered than subsurface rock masses exposed and transported during the failure.

Both the marble and schist are highly fractured (spacing <2 m) and weathered. Weathering grade, based on the classification of the Geological Society Engineering Group Working Party (1977), ranges from II to V, or slightly weathered to completely weathered, with most material moderately to highly weathered.

GSI values estimated at each outcrop range from 20 to 80 (Fig. 11). The marble outcrops have GSI values higher than 50 and an average value of 63, whereas the schist is considerably weaker, with an average GSI value of 39 and a minimum range of 20-30. One 50-cm-thick shear zone consisting of weak, soil-like material has an average GSI of 45-55.

We estimated rock strength using a geological hammer and Schmidt Hammer according to the guidelines in Hoek and Brown (1997) and British Standards (2015). These field estimates of strength were required because only a limited number of rock samples could be collected and analysed for laboratory point load testing. Schmidt Hammer rebound values range from <20 to 62. Most in situ intact rocks tested have approximate unconfined compressive strengths (UCS) of 100 MPa or greater. The weakest rock type, a schist unit outside the landslide area, has an estimated UCS of 35–50 MPa. These values were used as approximate estimates of the upper bounds for rock strength.

Of the 53 point load tests conducted on samples in the laboratory, 23 were schist and 30 were marble. The laboratory results generally agree with the field intact rock strength estimates. The point load $I_{s(50)}$ values of the marble and schist samples range from 0.2 to 8.5, and the corresponding UCS strength values from 4 to 188 MPa. Approximately 75 % of the UCS values are lower than 100 MPa. We attribute low strength values to the highly weathered and fractured nature of both rock types. We considered anisotropy of the schist and marble by testing samples parallel and perpendicular to foliation and bedding, but the results were statistically insignificant based on simple *t* tests. Hence, the foliation of the schist does not seem to be significant in strength considerations at the laboratory scale. Given the variability in the rock masses, the estimated UCS values from the point load tests, together with typical values from the literature (Bell 1994; RocData, Rocscience 2013), were used to derive input data for subsequent numerical modelling.

4.3 Two-dimensional Dynamic Numerical Simulations

The rock mass characterisation and reconstruction of the 1959 catastrophic failure presented in the previous sections was largely based on field investigations. However, in seeking to understand the detailed conditions and processes that led to slope failure during the Hebgen Lake earthquake, we had no direct observations, and thus had to rely on numerical simulations. We used a suite of two-dimensional numerical models to investigate possible roles of wave amplification and repeated seismic loading as contributors to failure initiation. First, we used purely elastic models to explore the magnitude of wave amplification related to topography, to compliant discontinuities such as the open tension cracks and the sliding surface, as well as

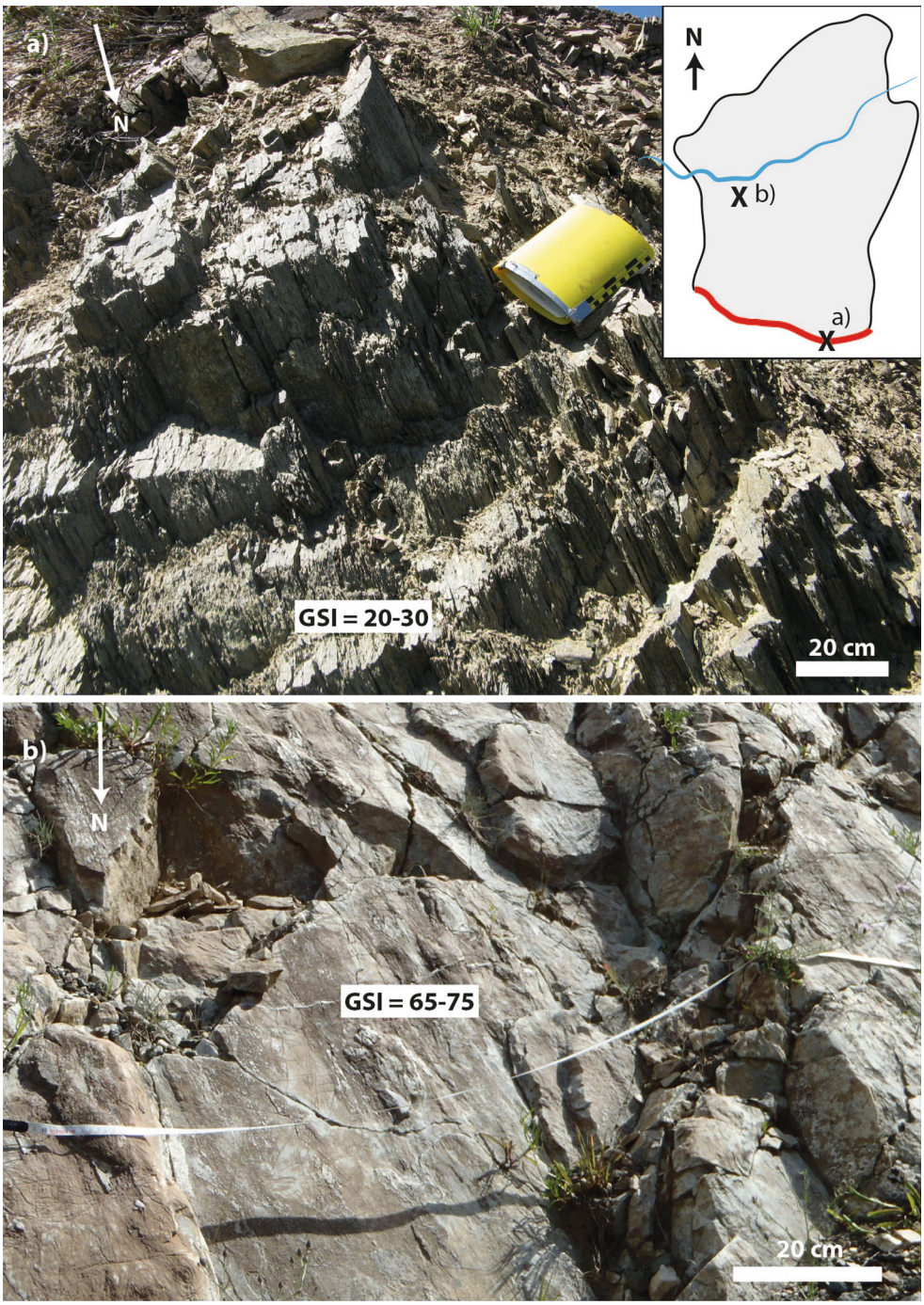

Fig. 11 Geological Strength Index (GSI) ranges for **a** a weak schist sequence at headscarp zone E and **b** the remnant dolomitic marble outcrop at the base of the slope. *Inset* shows the locations of outcrops; the *grey polygon* is the Madison Canyon landslide; the *red curve* is the headscarp; the *blue curve* is the Madison River (colour figure online)

to the material contrast at the marble-schist boundary. Second, we back-calculated strength properties required for failure after a single earthquake or a suite of earthquakes that progressively weakened the rock mass.

4.3.1 Models to Investigate Slope Amplification

Results of the dynamic models of Madison Canyon rock slope illustrate that three factors influence amplification: (1) slope geometry or topography, (2) discontinuities, and (3) material contrasts. We found that topographic amplification was always highest at the ridge crest (if discontinuities or material contrasts are absent), regardless of geometry, consistent with results of studies in other areas (Harp and Jibson 2002; Havenith et al. 2003a, b; Sepúlveda et al. 2005; Meunier et al. 2007, 2008; Bourdeau and Havenith 2008; Del Gaudio and Wasowski 2011; Gischig et al. 2015a, b). Peak amplification occurred at ~6.3 Hz

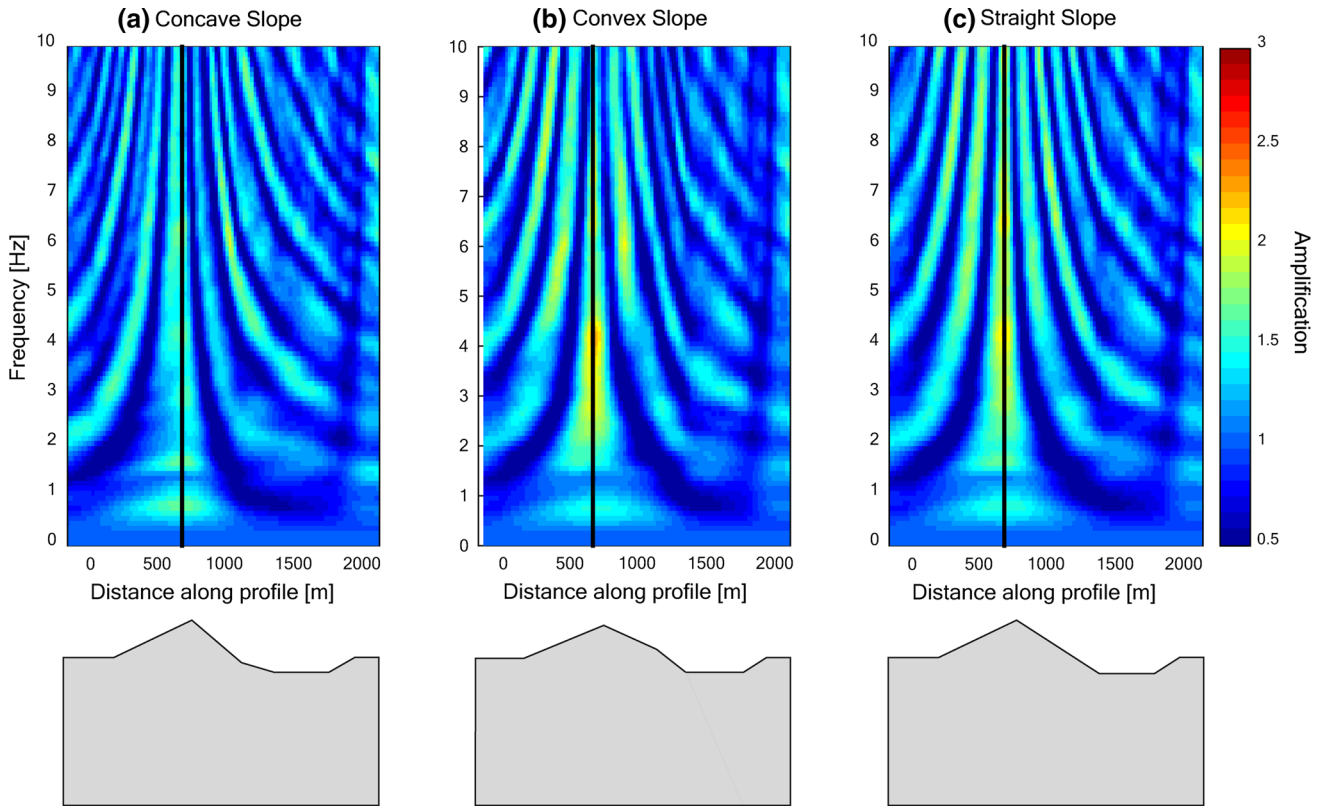

Fig. 12 Amplification field plots for the **a** concave, **b** convex, and **c** straight slope geometries. The block models at the base of each plot show the model geometry related to each amplification plot and have the same horizontal scale as the *x* axes of the amplification plots. The *black line* in each graph represents the crest of the slope (see Fig. 13) (colour figure online)

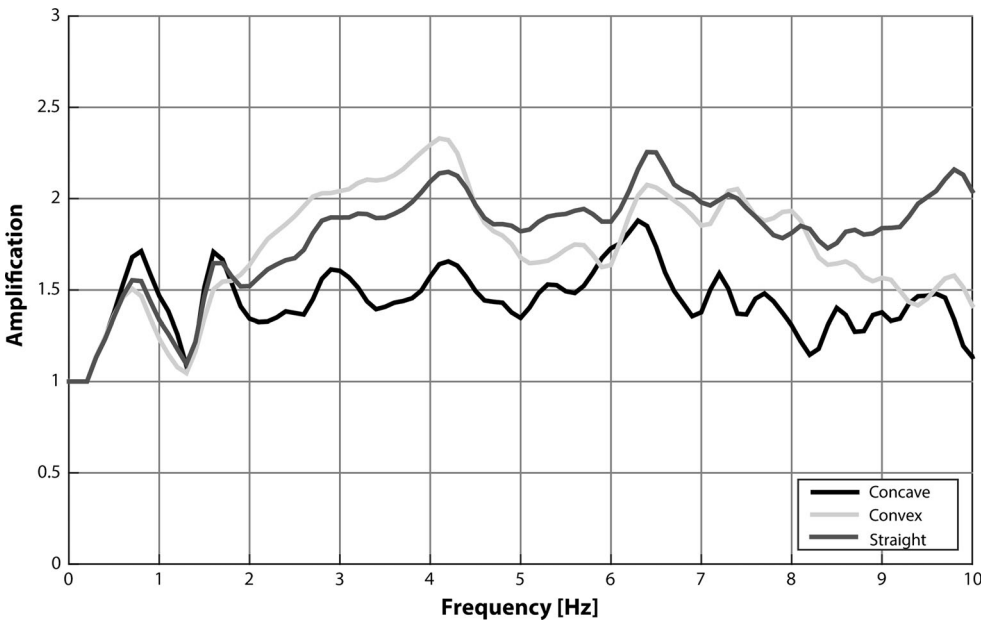

Fig. 13 Amplification graphs in the frequency domain for the concave, convex, and straight slope geometries at the ridge crest

for the straight and concave models, and at ∼4.1 Hz for the convex model (Figs. 12, 13). The concave slope simulations show the least amplification (<2×) relative to the input wave, and the convex slope simulations show the highest amplification (∼2.3×). These purely topography-related amplification factors agree well with the results of Ashford et al. (1997), Damjanac et al. (2013), and Burjanek et al. (2014) for rock slopes and open pits. The observed

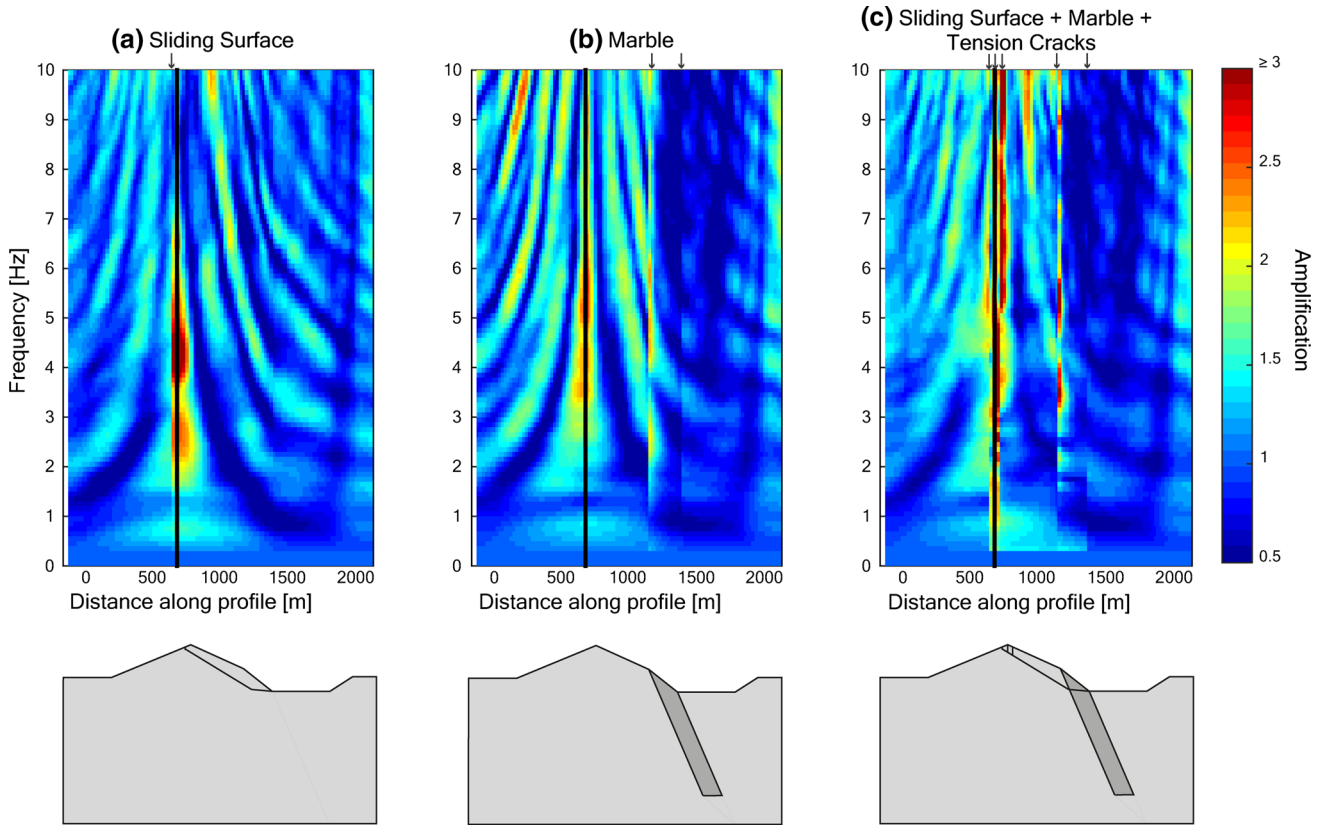

Fig. 14 Amplification field plots for the convex slope simulations including **a** the sliding surface only; **b** the marble contacts and material only; and **c** the sliding surface, marble contacts, and tension cracks. The block models at the base of each plot show the model geometry related to each amplification plot and have the same horizontal scale as the *x* axes of the amplification plots. The *black line* in each graph represents the crest of the slope (see Fig. 15), and *arrows* indicate traces of discontinuities in the amplification field plots (colour figure online)

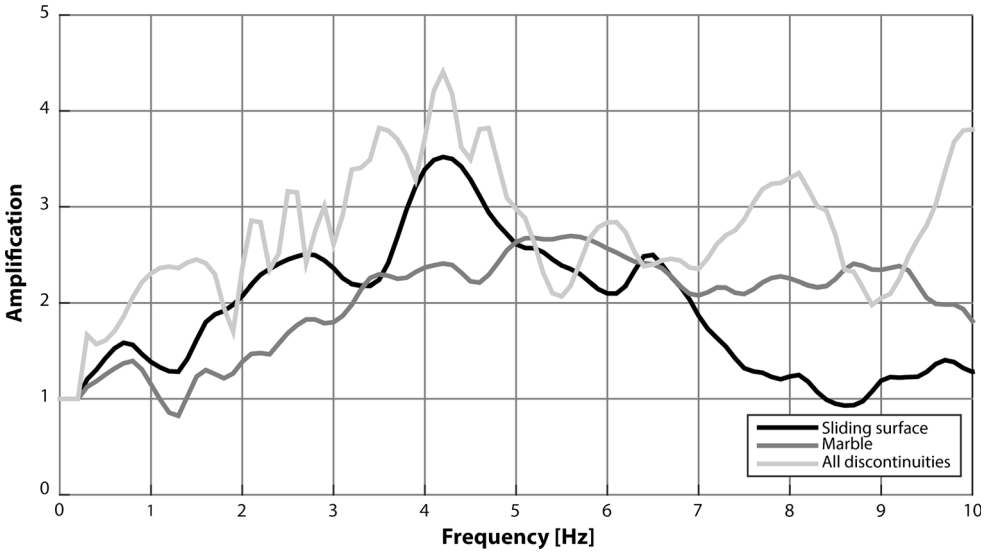

Fig. 15 Amplification graphs in the frequency domain for the sliding surface, marble, and all discontinuities simulations at the ridge crest

amplification pattern in Fig. 12 is the result of complex wave interaction that includes eigenmode vibration of the ridge as well as interference between incident, reflected, and Rayleigh waves generated at the inclined slope surface.

There is a significant increase in maximum amplification when the assumed sliding surface and tension cracks are included in the convex models as highly compliant discontinuities (Fig. 14)—from 2.3× to 3.5× for the sliding

surface simulations, and from 2.3× to 4.4× for the sliding surface, tension crack, and marble contact simulations (Fig. 15). The amplification field also shows clear breaks at the locations of daylighting discontinuities. For example, amplification at the leftmost discontinuity in Fig. 14c is >2× compared to 1.5× to the left of the discontinuity. The locations and spacing of daylighting discontinuities on the slope also appear to impact amplification. When only the sliding surface is included in the model, the contours of highest amplification are broader (~200-m wide) and smoother than when tension cracks and marble contacts are included. Maximum amplification for the sliding surface simulations occurs at approximately 4–5 Hz. In contrast, the tension crack models show more dispersed and complex amplification—maximum amplification occurs at 4 Hz, but there are also peaks at 3.5, 8, and 10 Hz at the crest of the slope (Fig. 14c, 15).

Another effect of discontinuities in the simulations is the broadening of the high amplification signal in the frequency domain. Setting an arbitrary lower bound of 2× amplification, the non-jointed convex slope model only exceeds this threshold over the 2.6–4.5 Hz range (Fig. 13). The jointed models all exceed 2× amplification over at least a 5 Hz interval (for example, the sliding surface model shows >2× amplification from 2 to 7 Hz) (Fig. 15). Hence, the high amplification signal is more dispersed in the jointed models.

Finally, models in which the schist and marble were included show further complexity in amplification patterns (Fig. 14b, c). There is a shift in amplification contours and surface wave patterns when the wave enters the marble, and high amplification contours appear on the upslope contact. The changes in amplification patterns are not as clear as those related to discontinuities.

4.3.2 Slope Damage and Failure

Static and dynamic slope stability was studied by enabling failure along Voronoi contacts in the intact rock or pre-existing discontinuities. Static models showed that the Madison Canyon slope only failed under static conditions when very low strength properties ($c = 0$, $\varphi \leq 20^{\circ}$) were assumed along Voronoi or discontinuity contacts. This result strongly suggests that long-term seismic damage is an important component of the slope's evolution. The models without Voronoi polygons, or joint sets, do not fail with the higher strength properties used to investigate amplification. Thus, internal contacts or discontinuities within the failure mass are required for catastrophic failure.

Dynamic simulations of cohesion and friction angle sensitivity with a single earthquake allowed us to constrain the peak strength values of the Voronoi contacts and of the discontinuities and sliding surface, assuming there was no pre-existing damage before the earthquake. These simulations provided a base for rock mass strength without seismic damage. For example, holding the peak friction angle for the Voronoi (vor) contacts and sliding surface (ss) constant at 40° and 35°, respectively, the slope fails (displacement >1 m) when $c_{vor\_peak} \leq 3.5$ MPa and $c_{ss\_peak} \leq 0.35$ MPa. At corresponding values of at least 4 and 0.4 MPa, the slope is stable (maximum displacement = 0.01 m after the earthquake and re-equilibration of the model). The friction angle sensitivity analyses indicate that, when cohesion is constant at 4 MPa (Voronoi contacts) and 0.4 MPa (sliding surface discontinuity), the slope fails with peak friction angles lower than 40° (φ_{vor_peak}) and 35° (φ_{ss_peak}) when residual friction angles are low (5°–15°) (Fig. 16; Table 6). Figure 16 shows the effect of the residual friction angle value. When it is low, as in the Voronoi (vor) results shown in Fig. 16, there is a distinct clustering of stable (maximum displacement <0.1 cm) and unstable (maximum displacement >1 m) results. Conversely, when the residual friction angle is 5° lower than the peak value, as in the DS model results in Fig. 16, there is more of a linear trend. The graph also indicates that Voronoi and DS friction angles are not as significant as the sliding surface friction angle. For example, when $\varphi_{ss\_peak} = 35^{\circ}$, a change in φ_{DS_peak} does not significantly influence maximum displacement or fractured contacts. However, when the φ_{ss_peak} is reduced by 10° or 15°, the models are unstable (high displacements) and more fractures form.

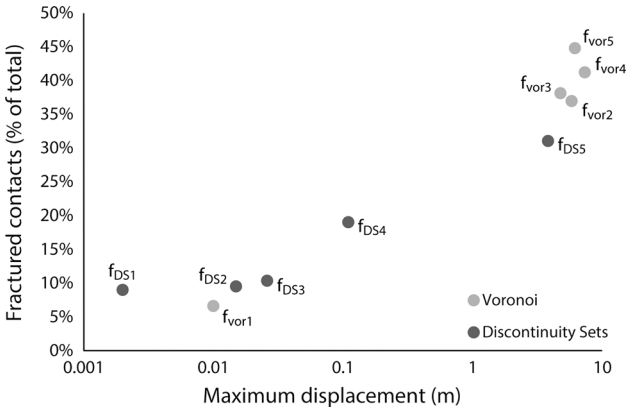

Fig. 16 Graph of maximum displacement versus fractured contacts (represented as the percent of total contacts in each model) for the friction (f) sensitivity analysis models. Model numbers correspond to those in Table 6. The Voronoi model results shown are for simulations with low (5°) residual friction angles. The DS model results are those of the simulations with high (5° less than peak) residual friction angles

The sensitivity analyses suggest a range in cohesion and friction angle values that is particularly susceptible to the development of new fractures. At strength values above this range, the number of new fractures drops off

Table 6 Sample results of the friction (f) sensitivity analyses (see Fig. 16)

Model	φ_{vor/DS_peak} (°)	φ_{ss_peak} (°)	Maximum displacement (m)	Fractured contacts (% of total)
f_{vor1}	40	35	0.01	7
f_{vor2}	35	35	5.8	37
f_{vor3}	30	35	4.75	38
f_{vor4}	25	35	7.33	41
f_{vor5}	15	35	6.14	45
f_{DS1}	40	35	0.002	9
f_{DS2}	35	35	0.015	9
f_{DS3}	30	35	0.026	10
f_{DS4}	40	25	0.11	19
f_{DS5}	40	20	3.81	31

Model numbers correspond to those in Fig. 16

vor/DS_peak peak values of the Voronoi or DS joints, *ss_peak* peak values of the sliding surface

dramatically and the slope is stable. At strength values below this range, the number of new fractures decreases slightly. This trend suggests that as the discontinuities become weaker, the internal deformation (new fracturing within the sliding mass) required for failure reduces (see Havaej et al. 2015).

The result of a sequence of earthquakes on the stability of the slope depends strongly on the strength parameters used. Models with c_{ss_peak} values of 1 MPa or greater are stable after five earthquake inputs. In contrast, Voronoi and DS models with $c_{ss\_peak} = 0.25$ MPa and $c_{ss\_res} = 0$ MPa, and $\varphi_{ss\_peak} \leq 25°$ and $\varphi_{ss\_res} \leq 20°$, fail after only one earthquake (for example, Fig. 17). The sliding surface properties thus determine the stability of the slope.

A common element in both the sensitivity analysis and earthquake sequence models is the mode of failure. Most models show either little fracture development and stability, or a large number of fractures and large displacements.

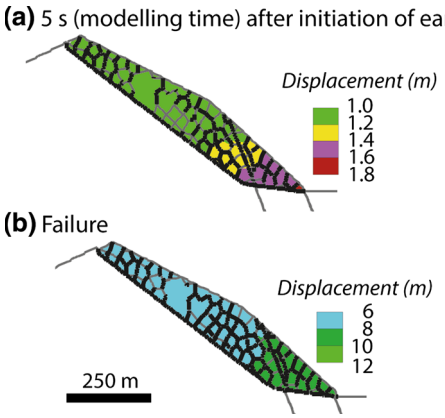

Fig. 17 Example of fracture development (in shear and tension) in a model with $c_{vor\_peak} = 2.5$ MPa, $c_{ss\_peak} = 0.25$ MPa, $\varphi_{vor\_peak} = 40°$, and $\varphi_{ss\_peak} = 35°$. The fractures developed as the first earthquake input (1994 Northridge) were applied to the model. *vor_peak* peak values of the Voronoi joints, *ss_peak* peak values of the sliding surface (colour figure online)

New fractures first appear on the sliding surface and on the upper marble/schist contact. Some fractures form at the ridge crest in the Voronoi models as well. In the model runs that lead to failure, numerous fractures then form in the marble and the schist near the ground surface. The last area of the sliding mass to develop fractures is the area behind the marble, half-way up the slope. The most abrupt failure occurs in models with low residual friction angles; more gradual, cumulative damage occurs in models with higher residual friction angles. This pattern is likely related to significant stress transfer in the models with low residual friction values, resulting in the rapid propagation of failure from localised fractures to rock mass collapse. Figure 17 shows an example of the development of fractures in a Voronoi model. The sliding mass initiates during one earthquake, with new fractures appearing first at the ridge crest and slope toe. At the end of the input earthquake record, almost all Voronoi contacts have failed in tension or shear, indicating a highly fractured sliding mass.

All model runs that lead to large-scale failure show the largest displacements in the toe area, where the marble is located. Independent movement of individual blocks is rare. Instead, the sliding mass moves uniformly showing some fragmentation (i.e. fractures develop along most Voronoi polygon or DS boundaries) (Figs. 17, 18).

The results of static and dynamic 2D simulations can be summarised as follows:

Under static conditions, the slope is stable. For catastrophic failure, but also for the formation of tension fractures that were observed before the 1959 failure, a strong external disturbance is required.

Topographic amplification alone is not a sufficient explanation for catastrophic failure at this particular site. However, local amplification is strongly enhanced close to compliant discontinuities (open tension cracks, pre-existing sliding surface) and the marble-schist contact.

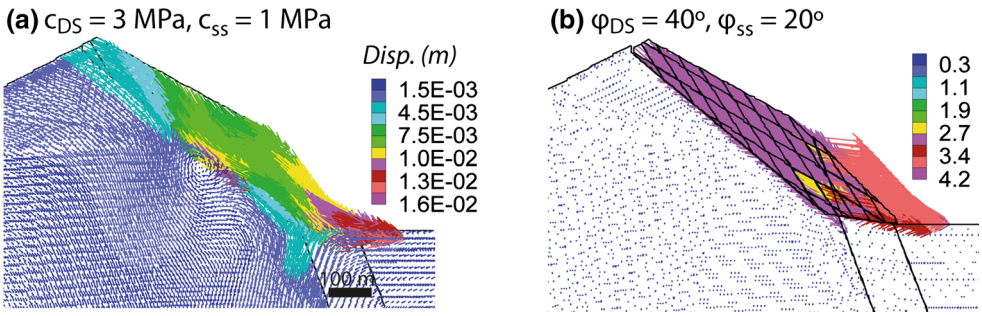

Fig. 18 Displacement vectors for the **a** c_{DS_peak} = 3 MPa (stable) and **b** φ_{ss_peak} = 20° (unstable) models showing movement initiation at the toe of the slope and uniform displacement. *DS* discontinuity sets, *ss* sliding surface (colour figure online)

Progressive damage accumulation due to repeated earthquakes may explain pre-failure tension fractures and rock mass weakening as suggested by Gischig et al. (2015a, b). However, depending on the strength parameters, failure occurs after a single earthquake or only limited damage is induced after five earthquakes. Damage accumulation is very sensitive to the residual friction along the sliding surface. Hence, a narrow range of combinations of strength properties, for which progressive rock mass weakening through repeated seismic loading occurs, may exist.

5 Discussion

5.1 Endogenic and Exogenic Processes

The south slope of Madison Canyon was conditioned for failure by endogenic and exogenic processes, including tectonic uplift of the Madison Range, previous earthquakes, erosion of the valley, undercutting of the slope by Madison River, gullying and other erosional processes on the slope, and weathering. The trigger for catastrophic failure was the 1959 earthquake. The effects of past earthquakes are apparent in offset fluvial terraces and exposed fault scarps. Madison River cuts through the Madison Range, keeping pace with tectonic uplift. Although glaciers did not directly affect the slopes in the slide area, their legacy of increased sediment loads affected Madison River and thus its capacity to erode the canyon walls in the slide area.

These processes, in combination with rock mass damage, progressively weakened the south slope of Madison Canyon and precipitated the 1959 failure. Their interaction caused microscopic and macroscopic fracturing of the rock masses, thus degrading their strength (cf. Leith 2012). The interaction between in situ stresses and exhumation and erosion of the landscape was significant in the development of the rockslide.

The role of exogenic processes in conditioning the Madison Canyon slope for failure is clear. The landslide occurred on a ridge at the west front of the Madison Range, in one of the narrowest reaches of Madison River, at the most significant knickpoint along the channel. River incision and undercutting of the south slope of Madison Canyon was an important factor in undermining the strength of the slope toe.

Rock mass damage due to the processes mentioned above is recognisable from slope morphology, differing GSI values, and block size. The area of highest tectonic and gravitational damage is the ridge crest, as indicated by the cluster of tension cracks, highly fractured rock, and thin (tens of centimetres) shear zones parallel to DS2 observed in the field. The contact between the schist and marble probably concentrated stress and hence tectonic damage and contributed to the release at the western margin the slide, due to moduli contrasts between the materials. Perhaps most importantly, the site of the failure was one where seismic energy was focussed, as revealed by the topographic amplification in the dynamic models.

5.2 Effects of Seismicity on Slope Stability

As mentioned above, seismicity is an important component of the history of the southern Madison Canyon slope. The 1959 earthquake triggered the catastrophic failure, allowing discontinuities to coalesce and form continuous sliding surfaces and fracturing the resistant marble buttress at the toe of the slope. However, past earthquakes, including the 77 historic events felt in the Hebgen Lake region, damaged and weakened rock masses prior to this event, possibly initiating extension at the ridge crest.

Through numerical simulations, we explored the interaction of the slope with seismic waves. Two-dimensional dynamic deformation analyses using UDEC provide an explanation for why the Madison Canyon landslide occurred on the south slope of Madison Canyon. Three aspects of the slope contribute to its uniqueness in the area: (1) slope geometry, leading to topographic amplification; (2) pre-existing tension cracks and fractures, leading to structural amplification; and (3) material contrasts between the marble buttress at the base of the slope and the schist-gneiss units above, resulting in material contrast amplification. The convex slope is located 30 km west of the

epicentre of the 1959 earthquake and faces NNW. The ridge changes orientation from NE-SW to WNW-ESE at the location of the landslide and then tapers to meet the wide, open Missouri Flats to the west. These geometrical characteristics amplified seismic shaking, focussing energy on the slope and thereby exacerbating the effects of the earthquake at this location.

The pre-existing tension cracks also altered seismic energy in the slope. In a hypothesised positive feedback system, previous earthquakes could have opened fractures at the ridge crest, leading to local amplification of the 1959 seismic energy in the slope. A similar hypothesis has been proposed for the Rawilhorn, Switzerland, slope (Moore et al. 2012). The contrast between schist and the marble buttress at the base of the slope also induced amplification.

Although seismic amplification is a component of the history of the slope, it alone did not cause failure. Amplification values, in the context of values cited in the literature, are not extraordinary. High amplification values associated with discontinuities or material contrasts do not involve large portions of the rock mass, but are localised. Hence, amplification may not be the only process promoting failure. In contrast, both pre-existing and cumulative damage were integral in bringing our models to failure. Whether we simulated the development of damage with low-strength parameters or by cycling through multiple earthquakes, the mode of failure remained the same. As mentioned above, most fractures in models that eventually failed developed in a short period of modelling time and the sliding mass failed rapidly, with movement initiating at the toe of the slope. Failure was particularly sudden and occurred after one earthquake input was applied in models with low residual friction angles (5°–15°), indicating that accumulating seismic fatigue is not as important in already weak rock masses. In models with higher residual friction angles, fracture formation occurred more gradually. Regardless of the rate of fracture propagation, fractures always initiated first on the assumed sliding surface and behind the upper marble/schist contact, and commonly at the ridge crest. Fractures then formed in the marble buttress. These modelling results help to explain the morphological evolution of the landslide noted on air photographs. Prior to 1959, the slope showed little deformation, with some extension at the ridge crest. The 1959 earthquake triggered failure in the schist and gneiss in the upper part of the slope and in the marble buttress at the toe of the slope. The resulting debris sheet, despite its comminution, preserved the integrity of the stratigraphy of the failed rock mass. Our models support these morphological observations. The displacement of the sliding mass initiated at the toe in the marble and propagated upslope, with individual blocks following each other sequentially, preserving the stratigraphy. The models also suggest that failure of the marble buttress is required for the landslide to happen. Hence, the marble is the determining factor—once it fractures and fails, it provides the kinematic freedom for the subsequent failure of the schist and gneiss.

The internal deformation of the modelled sliding mass is also an important factor in failure. Unlike landslides such as the Vajont Slide in Italy, which remained relatively intact during emplacement, the Madison Canyon landslide fragmented, showing brittle internal deformation. Our models indicate that, although the sliding surface played a dominant role in the landslide, many fractures developed in the sliding mass itself, suggesting that internal deformation could be a prerequisite for failure. Stress concentrations behind the marble buttress indicate more damage in that zone than in the midslope schist material above it. This internal damage is evidenced in the field by the high comminution observed in the deposits.

One limitation of the preliminary back-analysis models presented here is that we assumed Hadley's (1964, 1978) failure surface. Since his reports are from immediately after the catastrophic event, without subsequent deposition of secondary deposits, it is likely that his interpretations of the sliding surface are the closest to reality. However, future models may investigate the geometry of the sliding surface in more detail, using brittle fracture of intact rock to simulate the development of the surface. The fracturing in the Voronoi models is also an artefact of Voronoi contact locations, and should not be interpreted to signify exact fracture locations in reality.

5.3 Chronology of Events at Madison Canyon

From the geomorphological and structural evidence presented in this paper, we offer the following summary and chronology of events, illustrated graphically in Fig. 19:

1. Due perhaps to past earthquakes, tension cracks appeared in the south wall of Madison Canyon, indicating instability and possible partial formation of the rupture surface. The tension cracks formed in the low-strength schist-gneiss units, which had experienced slow continuous fatigue over time (Fig. 17). Based on our preliminary modelling results, pre-existing damage was essential to slope failure, while topographic amplification played a secondary role.
2. The 1959 Hebgen Lake earthquake triggered the catastrophic landslide. The rock mass on the west side of the slope appears to have failed first, probably at the base of the marble unit that formed a buttress on the lower part of the slope. Fragmenting marble acted as a layer on which the much larger mass of schist moved. The schistose debris also pushed the marble debris ahead of it to the distal limit of the landslide north of

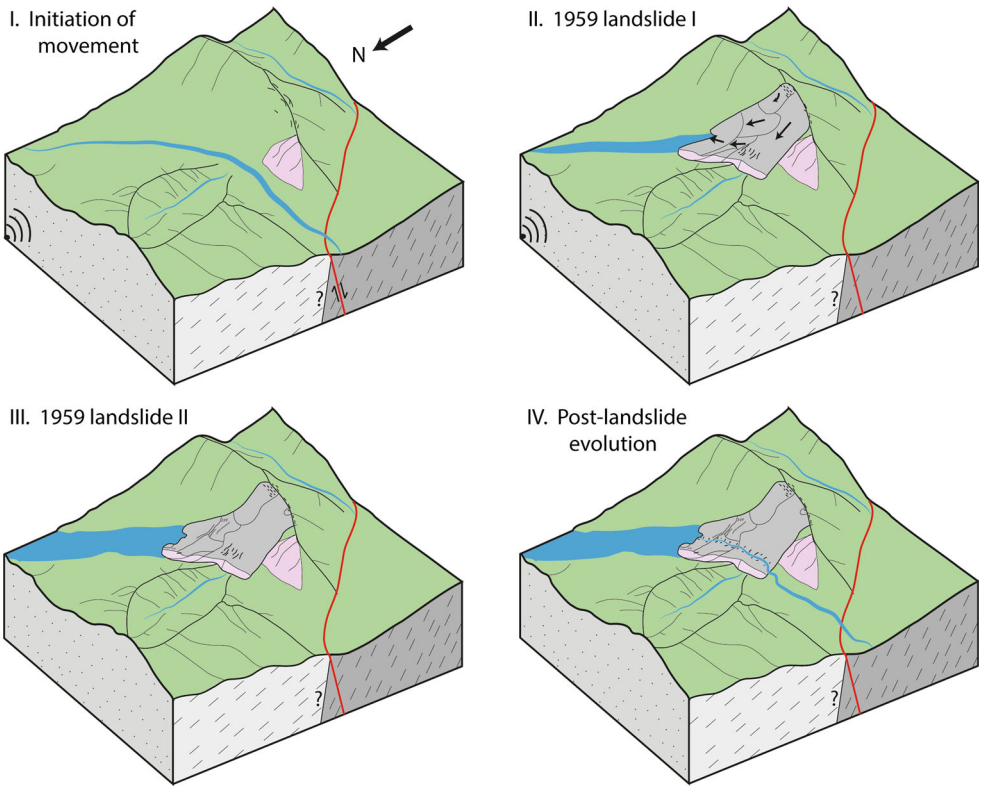

Fig. 19 Hypothesised sequence of events culminating in the catastrophic 1959 Madison Canyon landslide

Madison River (Fig. 5). The ribbon of marble debris that marks the outermost portion of the debris sheet was deformed by, and in places turned back into, the schist debris trailing it.

3. Shortly after the leading edge of the slide mass came to rest, the more coherent large blocks to the east, riding on highly comminuted debris, compressed as they encountered resistance from the marble debris and the rising slope north of Madison River (Fig. 6). The debris sheet then expanded into the valley. The coherent blocks still have trees on them, although most were toppled during transport. Late during or after the main landslide, a large secondary failure occurred from the headscarp on the east side of the slide. This slump regressed to the crest of the ridge. Several smaller rockfalls, slumps, and slides occurred in the days, months, and years following the main slide, particularly along the west lateral margin and below the headscarp. The catastrophic landslide dammed Madison River, forming Earthquake Lake, and altered the canyon mouth significantly.
4. Shortly after the 1959 landslide, the US Army Corps of Engineers constructed a channel through the slide debris to prevent collapse or overtopping of the landslide dam. The construction of the Earthquake Lake Visitor Centre further changed the morphology of the deposit. The deposit and headscarp have continued to evolve over the past 50 years (Fig. 8), with processes such as rockfalls and small slides transforming the slope. Deformation of the ridge crest continues, as evidenced by fresh tension cracks.

The above chronology highlights the complex evolution of the Madison Canyon landslide. In the west, it behaved like a rock avalanche with highly fragmented debris; farther east, large coherent blocks were transported on a layer of debris; a large slump followed the main event at the southeast corner of the landslide and several smaller failures occurred in response to the debuttressing of the slope. The marble unit at the base of the slope, which had buttressed the weaker schist and gneiss above, failed during the 1959 earthquake. The highly fractured state of the remaining outcrops indicates damage and fatigue due to weathering, erosion, and previous seismicity that conditioned the slope for failure.

6 Conclusions

We applied an integrated approach, including field and laboratory observations and measurements, long-range photogrammetry, air photograph interpretation, engineering geomorphological mapping, and 2D numerical modelling, to analyse the Madison Canyon landslide. We

constructed the first long-range terrestrial photogrammetry models of the failure, conducted engineering geological fieldwork to characterise the rock masses involved in the landslide, created detailed field and air photograph engineering geomorphologic maps, and simulated the event with 2D dynamic conceptual models.

This paper contributes to an improved understanding of the Madison Canyon landslide and other catastrophic failures by (1) showing the importance of endogenic and exogenic processes, including tectonic uplift and seismicity, fluvial erosion, and weathering, in preconditioning the slope for failure; (2) illustrating the importance of pre-existing and seismically induced damage and the secondary importance of seismic amplification for failure; and (3) determining a potential sequence of events during the catastrophic landslide, including the rapid fragmentation of the western rock mass, which flowed across Madison River, while largely intact blocks travelled to the northeast on a layer of finely crushed material.

The simulations presented in the paper are a preliminary application of a new approach to dynamic modelling and assume a discrete sliding surface. Future work could include simulating the formation of this sliding surface through brittle fracture of intact rock.

Acknowledgments The authors gratefully acknowledge the comments and advice of two reviewers and the help of the US Forest Service, particularly Joanne Girvin. Diane Doser supplied seismogram records. Camille Christiansen and Jeanette Klassen assisted in the field. Brent Ward helped with the air photograph analysis. The US Geological Survey provided imagery. Research was funded through an NSERC scholarship to A. Wolter and NSERC Discovery Grants to D. Stead and J. J. Clague.

References

Alzo'ubi AM (2009) The effect of tensile strength on the stability of rock slopes. PhD thesis, University of Alberta, Edmonton

Ashford SA, Sitar N, Lysmer J, Deng N (1997) Topographic effects on the seismic response of steep slopes. Bull Seismol Soc Am 87:701–709

Bell FG (1994) Engineering properties of soils and rocks, 4th edn. Blackwell Science, Oxford

Bourdeau C, Havenith H-B (2008) Site effects modelling applied to the slope affected by the Suusamyr earthquake (Kyrgyzstan, 1992). Eng Geol 97:126–145

British Standards Institute (2015) Description of soils and rocks, BS 5930. In: Code of practice for ground investigations. BSI Standards Limited, London

Brunsden D, Doornkamp JC, Fookes PG, Jones DKC, Kelly JHM (1975) Large-scale geomorphological mapping and highway engineering design. Q J Eng Geol 8:227–253

Burjanek J, Edwards B, Faeh D (2014) Empirical evidence of local seismic effects at sites with pronounced topography: a systematic approach. Geophys J Int. doi:10.1093/gji/ggu014

Damjanac B, Varun Lorig L (2013) Seismic stability of large open pit slopes and pseudo-static analysis. In: Dight PM (ed) Slope stability 2013. Australian Centre for Geomechanics, Perth, pp 1203–1216

de la Montagne J (1960) Geomorphic problems in the Madison Valley, Madison County, Montana: an introduction and synthesis. 11th annual field conference: West Yellowstone-Earthquake Area. Billings Geological Society, pp 165–169

Del Gaudio V, Wasowski J (2011) Advances and problems in understanding the seismic response of potentially unstable slopes. Eng Geol 122:73–83

Doornkamp JC, Brunsden D, Jones DKC, Cooke RU, Bush PR (1979) Rapid geomorphological assessments for engineering. Q J Eng Geol 12:189–214

Doser DI (1985) Source parameters and faulting processes of the 1959 Hebgen Lake, Montana, earthquake sequence. J Geophys Res 90:4537–4555

Fookes PG, Lee EM, Milligan G (eds) (2005) Geomorphology for engineers. Whittles Publishing, Caithness

Fookes PG, Lee EM, Griffiths JS (2007) Engineering geomorphology: theory and practice. Whittles Publishing, Caithness

Gao F (2013) Simulation of failure mechanisms around underground coal mine openings using discrete element modelling. PhD thesis, Department of Earth Sciences, Simon Fraser University, Burnaby

Geological Society Engineering Group Working Party (1977) The description of rock masses for engineering purposes. Q J Eng Geol 10:355–388

Geological Society of London (1982) Working party report on land surface evaluation for engineering purposes. Q J Eng Geol 15:265–328

Gerber E, Scheidegger AE (1969) Stress-induced weathering of rock masses. Eclogae Geol Helv 62:401–415

Giardino JR, Marston RA (1999) Engineering geomorphology: an overview of changing the face of earth. Geomorphology 31:1–11

Gischig V, Eberhardt E, Moore JR, Hungr O (2015a) On the seismic response of deep-seated rock slope instabilities—insights from numerical modelling. Eng Geol 193:1–18

Gischig V, Preisig G, Eberhardt E (2015b) Numerical investigation of seismically induced rock mass fatigue as a mechanism contributing to the progressive failure of deep-seated landslides. Rock Mech Rock Eng. doi:10.1007/s00603-015-0821-z

Griffiths JS, Whitworth M (2012) Engineering geomorphology of landslides. In: Clague JJ, Stead D (eds) Landslides: types, mechanisms and modelling. Cambridge University Press, New York, pp 172–186

Griffiths JS, Stokes M, Stead D, Giles D (2012) Landscape evolution and engineering geology: results from IAEG Commission 22. Bull Eng Geol Environ 71:605–636

Hadley JB (1964) Landslides and related phenomena accompanying the Hebgen Lake earthquake of August 17, 1959. US Geol Surv Prof Pap 435:107–138

Hadley JB (1978) Madison Canyon rockslide, Montana, USA. In: Voight B (ed) Rockslides and avalanches, 1. Elsevier Scientific Publishing, Amsterdam, pp 172–180

Harp EL, Jibson RW (2002) Anomalous concentrations of seismically triggered rock falls in Pacoima Canyon: are they caused by highly susceptible slopes or local amplification of seismic shaking? Bull Seismol Soc Am 92:3180–3189

Havaej M, Wolter A, Stead D (2015) The possible role of brittle rock fracture in the 1963 Vajont Slide, Italy. Int J Rock Mech Min Sci 78:319–330

Havenith H-B, Strom A, Jongmans D, Abdrakhmatov K, Delvaux D, Trefois P (2003a) Seismic triggering of landslides, part A: field evidence from the northern Tien Shan. Nat Hazards Earth Sys Sci 3:135–149

Havenith H-B, Vanini M, Jongmans D, Faccioli E (2003b) Initiation of earthquake-induced slope failure: influence of topographical

and other site specific amplification effects. J Seismolog 7:397–412
Hoek E, Brown ET (1997) Practical estimates of rock mass strength. Int J Rock Mech Min Sci 34:1165–1186
Hoek E, Kaiser PK, Bawden WF (1995) Support of underground excavations in hard rock. A.A Balkema, Rotterdam
Hoek E, Hutchinson J, Kalenchuk K, Diederichs M (2011) Appendix 3: Influence of in situ stresses on open pit design. In: Read J, Stacey P (eds) Guidelines for open pit slope design. CSIRO Publishing, Collingwood, pp 437–445
Itasca (2014) UDEC (v. 6.0). Itasca Consulting Group, Minneapolis
Jibson RW (2009) Using landslides for paleoseismic analysis. In: McCalpin JP (ed) Paleoseismicity, 2nd edn. Academic, New York, pp 565–601
Jibson RW, Rathje EM, Jibson MW, Lee YW (2014) SLAMMER—Seismic Landslide Movement Modeled using Earthquake Records (v. 1.1). US Geological Survey Techniques and Methods, Book 12, Chapter B1, unpaged
Kalenchuk KS, Diederichs MS, McKinnon S (2006) Characterizing block geometry in jointed rockmasses. Int J Rock Mech Min Sci 43:1212–1225
Kazerani R, Zhao J (2010) Micromechanical parameters in bonded particle method for modelling of brittle material failure. Int J Numer Anal Meth Geomech 34:1877–1895
Kent PE (1966) The transport mechanism in catastrophic rock falls. J Geol 74:79–83
Lee EM, Griffiths JS, Fookes PG (2004) Engineering geology: geomorphology. Encycl Geol 1:474–481
Leith KJ (2012) Stress development and geomechanical controls on the geomorphic evolution of alpine valleys. Dissertation, ETH Zürich, Zürich
Marinos P, Hoek E (2000) GSI: a geologically friendly tool for rock mass strength estimation. Proceedings of the GeoEng2000 at the international conference on geotechnical and geological engineering, Melbourne. Technomic Publishers, Lancaster, pp 1422–1446
Meunier P, Hovius N, Haines JA (2007) Regional patterns of earthquake-triggered landslides and their relation to ground motion. Geophys Res Lett 34:5
Meunier P, Hovius N, Haines JA (2008) Topographic site effects and the location of earthquake induced landslides. Earth Planet Sci Lett 275:221–232
Moore JR, Gischig V, Burjanek J, Löw S, Fäh D (2011) Site effects in unstable rock slopes: dynamic behaviour of the Randa instability (Switzerland). Bull Seismol Soc Am 101:3110–3116
Moore JR, Gischig V, Amann F, Hunziker M, Burjanek J (2012) Earthquake-triggered rock slope failures: damage and site effects. In: Eberhardt E, Froese C, Turner K, Leroueil S (eds) Landslides and engineered slopes. Taylor and Francis Group, London, pp 869–875
Murphy W, Mankelow JM (2004) Obtaining probabilistic estimates of displacement on a landslide during future earthquakes. J Earthq Eng 8:133–157
Murphy W, Petley DN, Bommer J, Mankelow JM (2002) Uncertainty in ground motion estimates for the evaluation of slope stability during earthquakes. Q J Eng Geol Hydrol 35:71–78
Rocscience (2013) RocData (v. 4.0). Rocscience Inc., Toronto
Saygili G, Rathje EM (2009) Probabilistically based seismic landslide hazard maps: an application in Southern California. Eng Geol 109:183–194
Sepúlveda SA, Murphy W, Jibson RW, Petley DN (2005) Seismically induced rock slope failures resulting from topographic amplification of strong ground motions: the case of Pacoima Canyon, California. Eng Geol 80:336–348
Shea T, van Wyk de Vries B (2008) Structural analysis and analogue modelling of the kinematics and dynamics of rockslide avalanches. Geosphere 4:657–686
Shelden AW (1960) Cenozoic faults and related geomorphic features in the Madison Valley, Montana. 11th Annual Field Conference: West Yellowstone-Earthquake Area, pp 178-184
Shugar DH, Clague JJ (2011) The sedimentology and geomorphology of rock avalanche deposits on glaciers. Sedimentology 58:1762–1783
Sturzenegger M (2010) Multi-scale characterisation of rock mass discontinuities and rock slope geometry using terrestrial remote sensing techniques. PhD thesis, Department of Earth Sciences, Simon Fraser University, Burnaby
Trunk FJ, Dent JD, Lang TE (1986) Computer modelling of large rock slides. J Geotech Eng 112:348–360
Wasowski J, Keefer DK, Lee C (2011) Toward the next generation of research on earthquake-induced landslides: current issues and future challenges. Eng Geol 122:1–8
Whalley WB (1974) The mechanics of high-magnitude, low-frequency rock failure and its importance in mountainous areas. Geographical Papers, University of Reading, Reading, pp 27–48
Wolter A (2014) Characterisation of large catastrophic landslides using an integrated field, remote sensing and numerical modelling approach. PhD thesis, Department of Earth Sciences, Simon Fraser University, Burnaby